Can atmospheric chemistry deposition schemes reliably simulate stomatal ozone flux across global land covers and climates?

Tamara Emmerichs[1], Abdulla Al Mamun[2], Lisa Emberson[3], Huiting Mao[4], Leiming Zhang[2], Limei Ran[5], Clara Betancourt[6], Anthony Wong[7], Gerbrand Koren[8], Giacomo Gerosa[9], Min Huang[10], Pierluigi Guaita[9]

[1]Institute of Energy and Climate Systems, Troposphere (ICE-3), Forschungszentrum Jülich, Germany, now at Max-Planck-Institute for Meteorology, Germany

[2]Air Quality Research Division, Science and Technology Branch, Environment and Climate Change Canada, Toronto, Ontario M3H 5T4, Canada

[3]Environment & Geography Department, University of York, York, UK.

[4]Department of Chemistry, State University of New York College of Environmental Science and Forestry, Syracuse, NY, 13210, USA

[5]Soil science and Resource Assessment, National Resource Conservation Service, U. S., Department of Agriculture, Raleigh, NC 27609, USA

[6]AXA Konzern AG, Cologne, Germany

[7]Centre for Global Change Science, Massachusetts Institute of Technology, Cambridge, MA, United States of America

[8]Copernicus Institute of Sustainable Development, Utrecht University, Utrecht, the Netherlands

[9]Dep.t of Mathematics and Physics, Catholic University of the Sacred Heart, Brescia, Italy

[10]Earth System Science Interdisciplinary Center, University of Maryland, College Park, MD, USA

Correspondence to: Tamara Emmerichs (tamara.emmerichs@gmx.de)

Abstract

Over the past few decades, ozone risk assessments for vegetation have evolved two methods based on stomatal O_3 flux. However, substantial uncertainties remain in accurately simulating these fluxes. Here, we investigate stomatal O_3 fluxes across various land cover types worldwide simulated by six established deposition models. Hourly O_3 concentration and meteorological data at nine sites were extracted from the Tropospheric Ozone Assessment Report database, a comprehensive global collection of measurements, for the model simulations. The models estimated reasonable O_3 deposition (0.5 - 0.8 cm s^{-1} in summer), which is mostly in agreement with the literature. Simulations of canopy conductance showed differences that varied by land cover type with correlation coefficients of 0.75, 0.80 and 0.85 for forests, crops and grasslands among the models. Differences between models were primarily influenced by soil moisture and vapor pressure deficit, depending on each model's specific structure. Across models, the range of O_3 damage simulations at each site was most consistent for crops (6 to 11 mmol O_3 m^{-2}), followed by forests (3 to 19.5 mmol O_3 m^{-2}) and grasslands (7 to 33 mmol O_3 m^{-2}). The median estimate across models aligns well with the literature at the sites most vulnerable to O_3 damage. Overall, this study represents a critical first step in developing and evaluating tools for broad-scale assessment of O_3 impacts on vegetation within the framework of TOAR phase II.

1. Introduction

Elevated surface O_3 levels significantly damage vegetation due to the stomatal uptake of O_3 by canopy leaves. Stomatal uptake of O_3 leads to plant tissue injury which in turn causes changes in metabolic functioning, reducing photosynthesis and consequently plant growth and productivity (Mills et al., 2011; Emberson, 2020; Ainsworth et al. 2012; Fuhrer et al., 2016; Grulke and Heath, 2020). Such damage can have significant impacts on crop yields and quality, leading to economic losses and impacting food security in regions already facing scarcity (Avnery et al., 2011; Ainsworth et al. 2017; Ramya et al., 2023). There is an ever-growing body of observational evidence demonstrating a variety of O_3 impacts on different ecosystems (crops, forests, grasslands) in North America, Europe and more recently, Asia (Emberson 2020). Various indices assessing O_3 exposure to vegetation have been developed over recent decades with the stomatal O_3 flux (POD_y; phytotoxic ozone dose

over a threshold y) index found to provide better estimates of O_3 risk to vegetation than the more commonly used concentration-based exposure approaches (e.g., Accumulated Ozone over Threshold (AOT); growing season daylight mean O_3 concentration (M7, M12) (Mills et al., 2011; Avnery et al., 2011). A global overview of spatial distribution and trends using concentration-based metrics was provided in the first Tropospheric Ozone Assessment Report (TOAR) by Mills et al. (2018). During TOAR phase II (TOAR-II), here we conduct a flux-based analysis to ensure the most up-to-date vegetation metrics are provided through this community effort.

O_3 dry deposition to vegetation is in part determined by canopy-level O_3 concentrations. A significant fraction of O_3 uptake occurs through the plant stomata with the remainder depositing on plant cuticular surfaces and the under-storey vegetation and soil. The stomatal contribution can vary between 50 and 80%, depending on the factors controlling the partitioning of stomatal and non-stomatal uptake (e.g., Huang et al., 2022; Wong et al., 2022; Clifton et al., 2023). As such, quantifying canopy stomatal conductance is important for assessing the mass balance of atmospheric O_3 concentrations and its potential damage to vegetation. Both stomatal and non-stomatal processes can vary with environmental conditions such as humidity, solar radiation, temperature and CO_2 concentration as well as vegetation type and density (Clifton et al., 2020a). The occurrence of soil water deficit can also play a crucial role where soil water stress induces stomatal closure (Lin et al., 2020; Huang et al., 2022). There are two commonly used stomatal conductance (g_s) models - the empirical, multiplicative approach first developed by Jarvis (1976) and the semi-mechanistic coupled net photosynthesis-stomatal conductance models (A_{net}-g_s). The common Jarvis-type models (e.g. Emberson et al., 2000; Ganzeveld et al., 1995; Zhang et al. 2003), widely applied due to their simplicity and computational efficiency, correct a prescribed maximum stomatal conductance with the multiplication of different environmental factors (e.g., temperature, light, soil water and atmospheric moisture). The A_{net}-g_s models couple g_s to plant photosynthesis by calculating the net assimilation of CO_2 and estimating gs based on the resulting supply and demand of CO_2 (Farquhar et al., 1980; Goudriaan et al., 1985; Ball et al., 1987). A_{net}-g_s models involve multiple non-linear dependencies on soil water, humidity and temperature, among other factors defined by measurement constraints (Ball 1987; Leuning et al., 1997). Heterogeneity of stomatal deposition estimates over different land cover types is anticipated, but model uncertainty depends on the representation of the deposition mechanisms, model parameterisation and meteorological inputs (Hardacre et al., 2015; Clifton et al., 2020b; Huang et al., 2022; Khan et al., 2024). Broadly speaking, the pros and cons of these two modelling approaches will tend to depend on the aims of the risk assessment study, the extent of knowledge of the ecosystem being investigated and prevailing bio-climatic conditions. Jarvis-type models are arguably more suitable for studies where less is known about the eco-

physiology of the ecosystem since they do not require simulation of net photosynthesis which in itself is inherently difficult to model accurately. However, these models still need to be calibrated for the particular bio-climate of study to ensure temperature and VPD functions are suitable for the prevailing conditions. By contrast, A_{net}-g_s models may be more useful for studies where the physiological response to environmental conditions of the ecosystems is reasonably well understood as they can provide insight into not only pollutant deposition, but also how other environmental conditions in addition to pollution may limit plant growth and productivity more generally.

In this study, the stand-alone version of six O_3 deposition schemes, commonly used in climate or air quality models, are assessed with a focus on their stomatal uptake portion and resulting POD_y calculation. Using concurrent O_3 concentration and meteorological variable measurement data from the TOAR database enables us to conduct a detailed intercomparison of multiple deposition schemes by avoiding uncertainties arising from using different input data. For this study, various sites have been selected to represent different land cover types and climate regimes around the globe, focusing on sites where observational data are available for O_3 concentration. By assessing the model estimates of stomatal O_3 deposition at these different sites, we aim to identify key differences in model formulation and parameterisation that influence estimates of stomatal O_3 flux and consequent POD_y. The estimation of the stomatal uptake from water flux measurements taken from the FLUXNET database provides an additional observational constraint as well as an uncertainty estimate at each site.

Furthermore, sensitivity simulations allow us to investigate the variability of stomatal O_3 deposition and plant damage with key input parameters and land cover characteristics. Post hoc, plant damage will be calculated offline based on the POD_y simulated by different models and flux-response relationships, where appropriate. Ultimately, we aim to understand the key factors driving stomatal O_3 flux and thus POD_y and assess the O_3-induced potential for vegetation damage for different land cover types and global regions.

2. Methodology

2.1 Meteorological and O_3 data from the TOAR-II database

The web version of the DO_3SE model is coupled to the TOAR database, i.e. the required input data (Table 3) is automatically provided by the database at the respective modelling sites. The TOAR-II database (from now on TOAR) contains harmonised measurements of surface O_3 and its important precursors and key meteorological variables that can impact O_3 concentrations and stomatal O_3 uptake. As one of the largest collections of quality-controlled air pollution measurements in the world, it comprises ground-based station measurements of O_3 concentration at more than 22905 sites globally which cover different periods between 1974 and 2023. These have been collected from different O_3 monitoring networks (e.g., Clean Air Status and Trends Network, CASTNET), harmonised and synthesised to enable uniform processing. The data were selected for inclusion in the TOAR database based on an extended quality control; e.g., sites where the measurement technique changed with time have been excluded. Data errors remain but have been shown to have a minor impact (Schultz et al., 2017). The total uncertainty in modern O_3 measurements is estimated to be < 2 nmol mol-1 (Tarasick et al., 2018). The meteorological data (irradiance, air temperature, relative humidity, precipitation, air pressure, and wind speed) in the database stems from the fifth generation of ECMWF reanalysis (ERA5) for global climate (Hersbach et al., 2020). Data re-initialisation (of precipitation and radiation, Copernicus Climate Change Service, 2017) is bridged by (linear) interpolation. The Leaf Area Index (LAI) data in the database stems from the MODerate resolution Imaging Spectroradiometer (MODIS). TOAR data is freely, and openly available through a graphical user interface and a representational State Transfer interface (https://toar-data.fz-juelich.de/api/v2/, last access: 01.11.2024). The TOAR data centre team is committed to the Findability, Accessibility, Interoperability, and Reusability principles (Wilkinson et al., 2016). The centre aims to achieve the highest standards regarding data curation, archival, and re-use (Schröder et al., 2021). To conduct offline simulations with models in addition to Web-DO_3SE, the input data were extracted beforehand and proven for identicality. The additionally required data (Table 3) were extracted from the TOAR database and the MeteoCloud server (https://datapub.fz-juelich.de/slcs/meteocloud/index.html) at Forschungszentrum Jülich.

2.2 Observation-constrained stomatal conductance

To compare the modelled stomatal conductance with observational information, we prepared model input data at two sites (Hyytiälä, Harvard Forest) from the FLUXNET 2015 dataset (Pastorello et al., 2020), which is openly available under the CC-BY-4.0 data usage licence. Additional vegetation information for the model input (i.e., LAI, canopy height, and crop calendar data) was provided by the site project investigators. Then, we used the

canopy-scale stomatal conductance dataset, SynFlux version 2 to estimate G_{st} for two forest sites, US-Ha1 and FI-Hyy. While in SynFlux version 1, canopy transpiration is assumed to be equal to total latent heat flux SynFlux version 2 improved its previous estimations (Ducker et al., 2018) by using a machine-learning-based method (Nelson et al., 2018) to partition total evapotranspiration into surface evaporation and canopy transpiration. To train quantile random forest models to relate meteorological conditions with water use efficiency (derived from water and carbon fluxes), periods with minimal surface wetness were chosen during the growing season. These models were then used to back-calculate transpiration for the whole growing season. Instead of the total latent heat flux, the resulting transpiration estimate was used as an input to the inverse Penman-Monteith Equation, reducing the potential high bias in the stomatal conductance estimates in SynFlux version 1.

2.3 Summary of sites selected for deposition modelling

Nine sites (Table 1) were selected for this modelling work accounting for the following factors: i. geographical spread,including major continents with terrestrial vegetation; ii. land cover/use types, including the plant functional types (PFTs) which are important in terms of economy, food security, or biodiversity and for which we have fairly good knowledge of O_3 impacts ; iii. availability of meteorological and O_3 data from the TOAR database; iv. availability of observational data describing stomatal conductance of water vapour (g_{wv}) estimated from the FLUXNET measurements (Section 2.2); and v. location proximity to previous experiments that have investigated O_3 impacts on vegetation that can help interpret our model results.

Table 1. Sites selected for stomatal deposition modelling using data from the TOAR database grouped by continent. Sites that also have FLUXNET data are denoted by 'FN' and those with SynFlux data are denoted by 'SF'.

Site (TOAR station id, nearest FLUXNET site id)	Location, station altitude from TOAR	Köppen-Geiger climate classification	Vegetation details (LAI, canopy height in m)	Record (measurement heights in m)	References

Europe					
Hyytiälä, Finland (FI00621, FI-Hyy) FN & SF	61.8611 °N, 24.2833 °E, 104 m	Dfc	LAI: 2.9 Height: 23.3	O_3: 2014 (4) FLUXNET: 1996/04-2013/09 (14)	Chen et al. (2018); Junninen et al. (2009); Visser et al. (2021)
Grignon, France (FR04038, FR-Gri) FN	48.5819 °N, 1.833 °E, 165 m	Cfb	LAI: 4.3 Height: 3.5	O_3: 2013/2014 (3) FLUXNET: 2004-2014 (2)	Stella et al. (2013)
Castelporziano, Italy (IT0952A, IT-Cpz)	41.8894 °N, 12.266 °E, 19 m	Csa	LAI: 6.9 Height: 14.0	O_3: 2013/2014 (19.7) FLUXNET: 2013/2014 (10)	Gerosa et al. (2005, 2009); Fares et al. (2009, 2012); personal communications with Silvano Fares
Asia					
Amberd, Armenia (AM0001R)	40.3844 °N, 44.2605 °E, 2080 m	BSk (or Dfa)	LAI: 3.9 Height: 1.0	O_3: 2009/2010 (3)	
Pha Din, Vietnam (VN0001R)	21.5731 °N, 103.5157 °E, 1466.0 m	Cwa	LAI: 6.9 Height: > 10.0	O_3: 2015-2017 (12)	Pieber et al. (2023); Bukowiecki et al. (2018); Yen et al. (2013)
North America					
Quabbin Reservoir/Har	42.2985 °N, -72.3341 °E,	Dfb	LAI: 3.0 Height: 24.0	O_3: 2010-2012 (2)	Clifton et al. (2019, 2020b);

vard Forest tower, USA (25-015-4002, US-Ha1) FN & SF	312 m			FLUXNET: 1993-2012 (24)	Ducker et al. (2018)
Nebraska, USA (31-055-0032, US-Ne3)	41.3602 °N, -96.0250 °E, 400 m	Dfa	LAI: 1.7 Height: 2.5	O_3: 2010 (2) FLUXNET: 2013/04- (0.5)	Amos et al. (2005); Leung et al (2020)
South America					
Huancayo, Peru (PE0001R)	-12.0402 °N, -75.3209 °E, 3314 m	Cwb	LAI: 3.6 Height: 1.0	O_3: 2015 (6)	
Africa					
Mt. Kenya, Kenya (KE0001G)	-0.062 °N, 37.297 °E, 3678.0 m	Aw	LAI: 4.2 Height: 1.0	O_3: 2015 (unknown)	Henne et al. (2008a,b)

Table 2. Land cover type, species and growing season (where SGS = start of growing season and EGS = end of growing season) by site. The equivalent land cover type and soil texture data used by the models used in this study (Section 2.3) are also shown. MESSy does not consider different land cover types. Models that do not consider soil type (i.e. do not include an estimate of soil moisture influence on stomatal deposition) are marked with *.

Station site: land cover type (species) and	**Web-DO$_3$SE**	**TEMIR***	**NOAH-GEM**	**ZHANG***	**CMAQ**

growing season					
Hyytiälä, Finland: evergreen needleleaf forest (Scots pine) SGS=1, EGS=366	evergreen needleleaf forest, loam	evergreen needleleaf boreal forest	evergreen needleleaf forest, organic material	evergreen needleleaf forest	evergreen needleleaf forest, silty loam (peat)
Grignon, France: crops (rapeseed and wheat) SGS=304, EGS=571	winter wheat, loam	C3 crop	crops/ grassland mosaic, silt loam	crops	crops (wheat), silty loam
Castelporziano, Italy: evergreen broadleaf forest (laurel, abutus, broad-leaved phillyrea, holm oak, pine) SGS=1, EGS=366	evergreen broadleaf forest, loam	Evergreen broadleaf temperate forest	evergreen broadleaf forest, sandy loam	evergreen broadleaf forest	evergreen broadleaf forest, loamy sand
Amberd, Armenia: Grassland, mixed SGS=1, EGS=366	grassland, loam	grassland	grassland, loam	long grassland	grassland, loam
Pha Din, Vietnam: evergreen needleleaf forest SGS=1, EGS=366	evergreen needleleaf forest, loam	evergreen needleleaf temperate forest	evergreen needleleaf forest, clay	evergreen needleleaf forest	evergreen needleleaf forest, clay
Quabbin Reservoir/Harvard Forest tower, USA SGS=93, EGS=312	temperate mixed forest, loam	deciduous broadleaf temperate forest	deciduous broadleaf forest, sandy loam	deciduous broadleaf forest	deciduous broadleaf forest, sandy loam
Nebraska, USA: crops (maize/soybean rotation) SGS=132/148,	crops (maize, soybean), loam	C3 crop	crops/ grassland mosaic, silty	crops	crops (corn), silty clay loam

EGS=278/260			clay loam		
Huancayo, Peru: grassland SGS=1, EGS=366	grassland, loam	grassland	grassland, loam	long grassland	grassland, loam
Mt. Kenya, Kenya: grassland, shrublands SGS=1, EGS=366	grassland, loam	grassland	grassland, loam	long grassland	grassland, silty loam

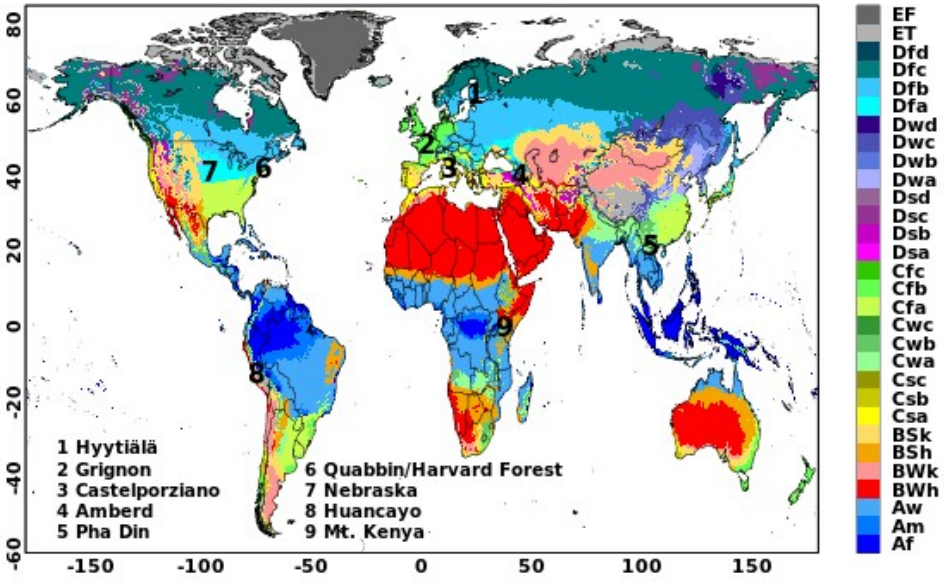

Fig. 1: Locations of 9 selected sites on Köppen-Geiger climate classification map for 1991-2020 (source: Beck et al., 2023). Table 1 specifies the classifications of these sites.

2.3 Stomatal deposition models and their key inputs

Six widely used empirical/Jarvis and semi-empirical/Ball-Berry types of stomatal deposition models were selected for this study. All of these used models can accommodate a variety of land cover/land use types and

provide estimates of stomatal deposition that can be output as both hourly- and season-long cumulative-stomatal deposition metrics. The key model features are described below.

(1) The empirical/Jarvis-type models use a predefined stomatal conductance modified with different environmental stressors for radiation (PAR), air temperature (T), vapour pressure deficit (VPD) and soil water (SM) - The ZHANG model (Zhang et al., 2002; 2003; 2006) and the Web-DO_3SE model (i.e., a version of DO_3SE that is directly coupled to the TOAR database, Emberson et al. 2000) account for sunny and shaded leaves (two-big leaf), the Web-DO_3SE model also depends on the vegetation phenology, the CMAQ_J model (Pleim and Ran, 2011) and the MESSy model (Ganzeveld et al., 1995; Kerkweg et al., 2006) account for one-big leaf CMAQ_J uses relative humidity (RH) instead of VPD. MESSy calculates the initial stomatal conductance based on the PAR and several empirical parameters

(2) Semi-empirical/Ball-Berry - The CMAQ_P model (Ran et al,. 2017) and the TEMIR model (Collatz et al., 1991; Farquhar et al., 1980) calculate the stomatal conductance at sunlit and shaded leaves for C3 and C4 plants depending on net CO_2 assimilation rate, CO_2 partial pressure, atmospheric pressure (Pa) and water vapor pressure for each leave. The NOAH-GEM model is different, calculating stomatal conductance at one big leaf using RH instead of VPD (Wu et al., 2011; Niyogi et al., 2009).

All models follow the resistance scheme:

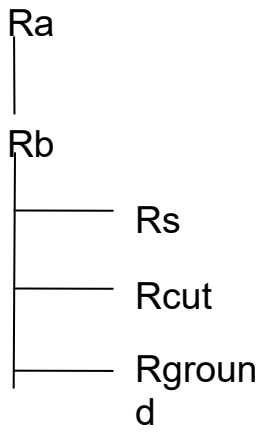

The land cover, growing season, and soil texture specifications used by the models are summarised in Table 2. For crops, we used the GGCMI Phase 3 crop calendar (Jägermeyr et al., 2021a) which provides the planting date and maturity day for 18 different crops at a 0.5° land grid cell resolution (Jägermeyr et al., 2021b). For forest trees, we consider four various classes: evergreen-needleleaf (EN), evergreen-broadleaf (EB), deciduous needleleaf (DN), and deciduous broadleaf (DB). For evergreen species, we assume a year-round growing season; for deciduous species, we use the simple latitude function described in Hayes et al.(2017); and we consider a year-round growing season for tropical species. The soil texture categories used by the models were obtained from the reference studies in Table 1 and the site principal investigators. Table 3 provides the key formulas, input data requirements and references for all models. Key total and stomatal deposition parameters for empirical models (g_{max}) and semi-empirical models (V_{Cmax}) are described in Table 4, which gives a good indication of the overall difference in the magnitude of stomatal deposition. The models' meteorological and O_3 inputs have been introduced in Section. 2.1.

Table 3. Stomatal deposition models selected for site-scale modelling (list of symbols: A1 and Section S3 in the SI, *uses u(h), o3(h)=1, for US-Ne: u(h), o3(h)=0.3).

Model	Approach	Key Formulas	Key Input data	Reference
ZHANG	Empirical (Jarvis-style)	$R_s = \frac{1}{\left[Gs(PAR)f(T)f(D)f(\psi) \times \frac{D_i}{D_v}\right]}$ $G_s(PAR) = \frac{L_{sun}}{r_s(PAR_{sun})} + \frac{L_{shade}}{r_s(PAR_{shade})}$	LAI, LUC, Wspeed, ssrd, T2m, Tskin, RH	Zhang et al., 2002; 2003; 2006

		$r_s(PAR) = r_{s,min}\left(1 + \frac{b_{rs}}{PAR}\right)$		
Noah-GEM	Semi-empirical, photosynthesis-based (Ball-Berry type)	$R_s = 1/\left[LAI\left(\frac{m A_n h_s P}{C_s} + b\right)\right]$	LAI, LUC, Wspeed, ssrd, strd, T2m, Tskin, RH	Wu et al., 2011; Niyogi et al., 2009
CMAQ_J	Empirical (Jarvis-style)	$R_s = \frac{r_{s,min} LAI}{\left(f_{PAR} f_T f_{vpd} f_w\right)}$	LAI, Tair, PAR, ssrd, rn, RH SM	Pleim & Ran 2011
CMAQ_P	Semi-empirical, photosynthesis-based (Ball-Berry type)	$R_s = 1/\left(\frac{m_g A_{net} e_s P_a}{C_s} e_i + g_0\right)$	LAI, CO_2, Pa, u*, h_dis, z0, SM, Tsoil, wspeed, wdir, Soil texture, C3/C4 type, PAR,	Ran et al,. 2017

			ssrd, rn, P_rate, sn, sd	
TEMIR	Semi-empirical, photosynthesis-based (Ball-Berry type)	$$R_s = \frac{1}{\left[\left(\frac{L_{sun}}{r_b + r_{sun}} + \frac{L_{shade}}{r_b + r_{shade}}\right)\frac{D_i}{D_v}\right]}$$ $$r_s = \frac{1}{g_s} = \frac{1}{\left[\alpha\left(\frac{m\,A_n\left(\frac{e_s}{e_{sat}}\right)}{\left(\frac{C_s}{P_{atm}}\right)}\right) + b\right]}$$	LAI, LUC, u*, ssrd, T2m, Tskin, RH, SM	Tai et al., 2024; Sun et al., 2022
MESSy	Empirical (Jarvis-style)	$$R_s = \left[r_s(PAR, LAI)\middle\vert f_T f_{vpd} f_w\right] \times \frac{D_v}{D_i}$$ $$r_s(PAR, LAI) = kc\,x \left[\frac{b}{d\,PAR}\ln\left(\frac{\exp(kLAI)+1}{d+1}\right) - \ln\left(\frac{\exp(-kLAI)}{d+1}\right)\right]^{-}$$	LAI, ssrd, RH, sw, Tir	Emmerichs et al., 2021; Kerkweg et al., 2006; Ganzeveld et al., 1998
Web-DO$_3$SE	Empirical (Jarvis-style)	$$r_s = g_{max}\,max\left\{\left(f_{min}, f_{temp}, f_{VPD}, f_{SWC}\right)\right\} \times f_{phen} \times f_{light}$$	Tair, VPD wspeed, P, Pa, O_3, Gr	Emberson et al., 2000; Bueker et al., 2012; Simpson et al., 2011; Guaita et al., 2023a

206

207

208 **Table 4 Model parameter V_{Cmax} at standardised temperature conditions (25°C) [in µmol CO_2 m^{-2} s^{-1}] and**
209 **g_{max} [O_3 in cm s^{-1}] for the total canopy by land cover/land use type. Note that the values presented in the**
210 **table were recalculated from the original respective rsmin values for H_2O (s m^{-1}) in ZHANG, MESSy, and**
211 **CMAQ_J, and Vc_{max} values for O_3 (mol O_3 $m^{-2}s^{-1}$) in Web-DO_3 SE .**

Parameter	**Web-DO_3SE**	**ZHANG**	**CMAQ_J**	**TEMIR**	**NOAH-GEM**	**CMAQ_P**
G_{max} or V_{Cmax}	g_{max} [cm s^{-1}]	g_{max} [cm s^{-1}]	g_{max} [cm s^{-1}]	V_{Cmax}^{+} [µmol CO_2 m^{-2} s^{-1}]	V_{Cmax} [µmol CO_2 m^{-2} s^{-1}]	V_{Cmax} [µmol CO_2 m^{-2} s^{-1}]
Forests	0.44 (EN) 0.49 (EB) 0.55 (DB)	0.25 (EN) 0.42 (EB) 0.42 (DB) Zhang et al., 2003	0.36 (EN), 0.53 (EB), 0.32 (DB), Pleim & Ran, 2011	60.1 (EN) 59.0 (EB) 55.4 (DB), (Oleson et al, 2013; NCAR Technical notes)	57.6 (EN) 96 (EB) 96 (DB) Niyogi et al., 2009; JAMC	57.6 (EN, Slevin et al 2015), 49.2 (EB, Medi. forest, (EB_tr+EB_te)/2,Oliver et al., 2022), 55.4 (DB, CLM4.5, Kattge 2009)
Crops	1.1 (wheat) 0.74 (maize) 0.73 (soybean)	0.53	0.91	96.7	76.8	96.7 (CLM4.5)

Grasses	0.66	0.64	0.64	75.1	28.8	75.1 (CLM4.5)

212

213 POD_y is calculated in post-processing, according to the guidelines in UNECE LRTAP (2017):.

214 $$POD_y = \sum_{i=1}^{n} \left[fst, sun_i - y \right] \times \left(\frac{3600}{10^6} \right) \quad \text{for } fst, sun_i \geq y nmol\, m^{-2} PLA\, S^{-1}$$

215 Where fst, sun_i is the hourly mean O_3 flux in nmol O_3 m^{-2} PLA s^{-1} at sunlit leaves, y is a species-dependent
216 threshold (crops: 6 nmol O_3 m^2 s^{-1}, grassland and forests:1 nmol O_3 m^{-2} s^{-1}; UNECE LRTAP (2017) and i is the
217 number of daylight hours (when ssrd > 50 W m^{-2}) within the accumulation period (growing season). The term

218 ($3600/10^6$) converts from nmol m^{-2} PLA s^{-1} to mmol O_3 m^{-2} PLA. fst, sun is calculated by:

219 $$f_{st,sun} = c \frac{(z) \times g_{st} \times r_c}{r_b + r_c}$$

220 Where c(z) is the O_3 concentration at in nmol m^{-3} (calculated from ppb by multiplying by P/RT where P is the
221 atmospheric pressure (Pa) and T is the air temperature (K), R is the universal gas constant of 8.31447 J mol^{-1} K^{-1}
222 and T is the assumed standard air temperature (293 K). The leaf surface resistance (r_c) is given by $r_c = 1/(g_{st}+g_{ext})$
223 where g_{ext} is the inverse of cuticular resistance.

224 . The leaf boundary resistance is calculated by:

225 $$r_b = 1.3 \times 150 \times \sqrt{\frac{L}{u(h)}}$$

226 Where factor 1.3 accounts for the differences in diffusivity between heat and O_3, L is the crosswind leaf
227 dimension (i.e. leaf width in m) and $u(h)$ is the wind speed at the top of the canopy.

228 **2.4 Description of stomatal deposition model simulations**

The result section aims at identifying trends in stomatal deposition models among different land cover types including grass, crops and forests using four model experiments as follows.

In experiment 1, the different models are driven by the O_3 and meteorological data from ERA5. We analysed the simulated deposition velocity (V_d) split into stomatal and non-stomatal fractions, canopy (G_{st}) and sunlit (G_{sun}) stomatal conductance.

To include observational constraints, in **experiment 2,** the TEMIR, ZHANG, NOAH, MESSy and CMAQ models were run with data obtained from the FLUXNET database (available for three sites, see Table 1), and the simulated G_{st} was evaluated with observation-derived values, inferred G_{st}, of SynFlux. Spearman correlation was applied for the model evaluation, as it can be applied to any datasets including non-parametric and non-linear ones. The US-Ha1 and FI-Hyy sites were considered for the model evaluation due to the availability of SynFlux data at these sites

A sensitivity analysis (**experiment 3**) was performed by driving a set of models with synthetic input data in the following steps: i. O_3 input was perturbed by +/- 40% (Sofen et al. 2016). ii. soil water content was perturbed by +/- 30 % (Li et al., 2020). iii. absolute humidity was perturbed by +/- 30%, soil and air temperatures were perturbed by +/-3, independently, iv. the growing season, which was mostly approximated by LAI, was shifted by 14 days forward and backward in time. In set (iii) and (iv), relative humidity was calculated from absolute humidity and temperature after their perturbation. In both cases, absolute humidity was capped at the saturation vapour pressure at the corresponding temperature.

Finally, for **experiment 4,** g_{max} and V_{Cmax} of the models were varied by +-20 %, based on previous estimates of plant traits dependent uncertainty (e.g., Walker et al., 2017; UNECE LRTAP, 2017).

3. Results

3.1 General characteristics of simulated total deposition velocity and stomatal contribution

The split of total O_3 deposition between different pathways, G_{st}, G_{cut}, G_{ground}, simulated by the 7 models is shown for each of the 9 sites in Figure 2 and S2 (corresponding data are presented in Table S9). This analysis allows us to briefly assess the overall efficacy of the model's ability to simulate deposition velocity V_d (by comparisons with previously published values; more complete assessments of model's ability for some of these sites can be

found in Clifton et al., 2023) and to compare the importance of the stomatal deposition pathway between models for different land cover types and across different seasons.

Observations of V_d have only been made at a handful of sites i.e. Hyytiälä, Finland; Castelporziano, Italy; Grignion, France and Harvard Forest, US (close to our Quabbin site in terms of proximity, land cover type and climate). Overall, the models capture V_d at these sites compared to observed values reported in previous studies. Namely, the observed seasonal cycle in V_d at Hyytiälä, Finland (needleleaf forest), with lows of ~0.1 cm s^{-1} between January and April and highs of 0.4 cm s^{-1} between June to September, averaged over 10 years of measurements from Clifton et al. (2023) and Visser et al. (2021) are captured by most models except of MESSy and TEMIR, which reach V_d values of 0.8 cm s^{-1} during the summer. Similarly, the strong seasonal cycle in V_d at Quabbin, US (temperate mixed forest), ranging from around 0.2 cm s^{-1} between January and April up to 0.5 cm s^{-1} from June to September in Clifton et al. (2023) is captured by all models. Observed V_d at Castelporziano, Italy (evergreen broadleaf forest) shows relatively constant values throughout the year, commonly between 0.4 and 0.8 cm s^{-1} averaged over a 2-year period (Savi & Fares, 2014). The study by Stella et al. (2011) reports V_d measurements of 0.63 cm s^{-1} (on average) at Grignion (France). At the other sites, no O_3 dry deposition measurement exists and thus we report the observed ranges for the land cover type (and possibly the matching climate). Over grassland, Silva and Heald (2018, and references therein) show a mean of 11 measurements of daytime V_d values (~0.4 cm s^{-1}) in agreement with our models. Measurements exist at soybeans and maize crops which indicate V_d values of 0.7 (Meyers et al., 1995) and 0.4 - 0.6 cm s^{-1} (Stella et al., 2011), respectively. Thus, the models seem to estimate too low deposition at soybeans.

In terms of deposition pathways, for all sites and models, stomatal deposition consistently ranks as the most important pathway in the summer, whereas in winter and, for some models, in the fall G_{st} decreases to zero to very low at sites with seasonal variation in vegetation coverage. The importance of the pathway varies with land cover type and season. The highest stomatal contribution of 90 % (NOAH model) is shown at the Amberd site. Among the different land cover types, the highest average stomatal contribution to deposition during the summer is estimated across grass (67 %), followed by crops (65 %) and forests (59 %). The seasonal importance of stomatal contribution is not seen for the tropical sites as the year- round growing season means that stomatal conductance is driven by solar radiation which is constant throughout the year (e.g. Hardacre et al., 2015). Previous studies involving measurements and partitioning approaches (Horvath et al., 2018, Meszaros et al., 2009) indicate that the non-stomatal O_3 deposition pathways (i.e., G_{ground} and G_{cut}) are very strong (in some cases, dominant over G_{st}) at short vegetation such as the grasslands. Despite there are multiple factors such as wind

speed, solar radiation, LAI, etc., that control the relative contributions of the three deposition branches, G_{st} is the dominant pathway at the three grassland sites of the current study (Amberd, Mt Kenya, and Peru). At the Amberd and Peru sites, G_{cut} and G_{ground} are small since low wind speed reduces downward mixing of ozone to the surface (atmospheric resistance, e.g., at the Peru Site in the Summer season, the mean wind speed was 1.0 cm s^{-1} and the G_{cu} and G_{ground} contributions in the TEMIR model were 21 % and 12 %, respectively; Table S3).

In contrast, at the Mt Kenya site, G_{st} exceeds G_{cut} and G_{ground}, since the strong solar radiation (annual mean is 246 W m^{-2}, Table S2) at this site favours stomatal opening . Besides that, LAI is a very important governing factor for G_{st} . Therefore, it can be inferred that the O_3 deposition pathway depends on not only the land cover type but also meteorological drivers. The relative contributions of each deposition pathway depends on the interplay between these key factors at a particular site. Among the models, Web-DO_3SE estimated the lowest stomatal contribution at grass (Fig. 2) most likely due to its parallel pathways to cuticle, soil and stomata, with the former scaled by LAI with a constant cuticular deposition of 2500 s m^{-1}. Such differences in model structures likely led to the wide-ranging partitioning. For example, for the Quabbin site (summer), all models simulate G_{cut} ranging from 15-65 %, G_{ground} from 2-19 % and G_{st} from 33-66 % despite their agreement on the overall V_d values (total bar). Models agree better in the partitioning of O_3 dry deposition to crops with summer stomatal fraction contributions ranging between 46-73 %, 37-73 % and 51-81 % for US-Ne3 Maize, US-Ne3 soybeans and FR-Gri (rapeseed and wheat). Most models estimate non-stomatal deposition equal to or larger than the stomatal contribution to deposition outside of the tropics in winter and fall, and to some extent in spring. This again emphasises the importance of the stomatal contribution to the seasonal cycle of total deposition as also found in Clifton et al. (2023). Similarly, as seen at grasslands, Web-DO_3SE (Fig. 2, Table S3) accounts for the highest non-stomatal deposition at crop sites.

Across all forest sites, models show significant cuticular uptake throughout the year ranging between 11 % and 94 % contribution. At FI-Hyy, G_{cut} averages ~50 % across all seasons and all models with higher estimates of ~55 % by the TEMIR model due to the higher wind speed at FI-Hyy (annual mean wind speed is 3.2 m s^{-1}; Table S2) favoring cuticular deposition as suggested by Rannik et al. (2012). At IT-Cpz, our models estimate on average around 43 % (20-80 %) to be non-stomatal deposition, close to the previously reported ranges (Gerosa et al. 2005, Fares et al. 2012, Fares et al. 2014), which were up to 57 % from non-stomatal deposition and 30-60 % from stomatal uptake. A similar partitioning (59 % G_{st}, 33 % G_{cut}, 5 % G_{ground} model average in summer) is seen at PhaDin.

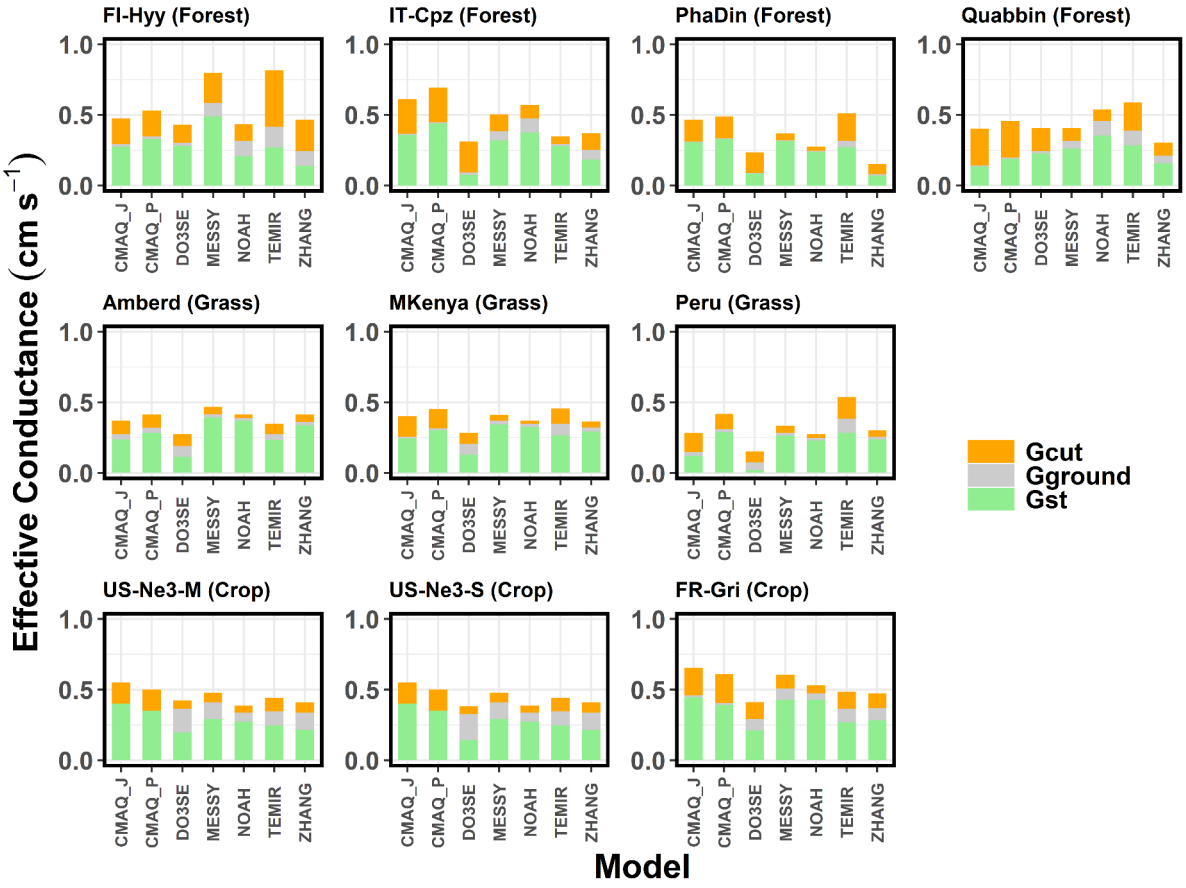

315

316 **Fig. 2 Mean effective conductanceof the cuticular (G_{cut}), ground (G_{ground}), and stomatal (G_{st}) deposition**
317 **pathways of O_3 across various models and sites during the summer season (US-Ne3-S=soybeans, US-Ne3-**
318 **M=maize). Respective figures for the other seasons are presented in the supplement.**

319

320 All models except Web-DO$_3$SE were compared on a seasonal and hourly basis with the SynFlux G_{st} data for US-
321 Ha1 and FI-Hyy sites (Figures S2, S3). CMAQ_J, NOAH, TEMIR, and ZHANG show reasonable agreement at
322 the Quabbin forest (US-Ha1) whereas CMAQ_P and MESSy show quite significant overestimates at both FI-
323 Hyy and Harvard Forest (Table S5) and CMAQ_J overestimates at FI-Hyy only. Note that NOAH and ZHANG
324 show significant underestimates at FI-Hyy while agreeing well with SynFlux at Harvard Forest (Quabbin). The

underestimates by the ZHANG model are consistent with the results from a similar comparison for Yellowstone National Park in the US by Mao et al. (2024). Compared to Harvard Forest, FI-Hyy is the most humid and cloudy with the lowest solar radiation flux, and these conditions likely contribute to the underestimates by the NOAH and the ZHANG model as identified by Mao et al. (2024). The differences between modelled and SynFlux G_{st} do not seem to be associated with the model types, i.e. empirical or photosynthesis-based models.

The correlation of the diurnal cycle of G_{st} calculated by the models with the inferred G_{st} by SynFlux for US-Ha1 and FI-Hyy (Fig. S4) confirms that models generally capture the temporal patterns of G_{st} of at least these two different forest types and climates (FI-Hyy: EN, temperate, subarctic; Quabbin: DB, moist temperate). The best Spearman correlations are found at FI-Hyy and range between 0.73 by the MESSy model and 0.85 by the TEMIR model. Overall lower correlations are found at the Quabbin site ranging from 0.65 for the NOAH and MESSy models to 0.82 for the CMAQ_P model. This poorer correlation suggests that additional water stress may limit stomatal conductance at Quabbin, which the models do not capture, compared to FI-Hyy. Notably, a similar range of correlation coefficients (0.61 – 0.93) was found when modelled G_{st} values obtained using the TOAR input data were compared with SynFlux G_{st}. As SynFlux data were generated using FLUXNET measurement data, this result corroborates the validity of using the TOAR database as input to Web-DO_3SE, developed as a service website to aid in risk assessment of O_3 damage to European vegetation.

To identify the key drivers of the G_{st} model schemes among different land cover types and climate conditions, we also compare estimates of G_{st} between models for all sites and analyse the similarity of G_{st} diurnal cycles in empirical and photosynthesis models. Here, it is important to understand the model distinction between shaded and sunlit leaf (G_{sun} , Fig 4). The average diurnal variations of stomatal conductance (G_{st}) of O_3 at the 9 sites for each season are shown in Figure 3 and S7. This also helps interpret the modelled stomatal conductance of sunlit leaves (G_{sun}) shown in Fig 4 and S8. Across all models, the diurnal mean G_{st} (Fig. 3) varied from 0.15 cm s^{-1} (Quabbin) to 0.50 cm s^{-1} (Mt. Kenya). In the TEMIR and the ZHANG model, roughly 50% of G_{st} occurs at the sunlit part of the leaves. Web-DO_3SE and CMAQ_P G_{sun} contribute 30 % on average (Fig. 4). At mid-to-high latitudes, the model spread is limited to the summer season, whereas at tropical sites, it is similar throughout the year. During the day, models show a spread of 1.2 cm s^{-1} in G_{st} at the forest and grassland sites during the summer while their predictions agree most at the crop sites (throughout the year) with a maximum of 1.0 cm s^{-1}. This is due to the flux response relationship which has a more sensitive response (steeper slope for most crops) due to a higher threshold (see Table 5 for the equations describing the steepness of the change). Results among

the same model type differed significantly while different model types could produce similar results at the same location. For the sites with distinct seasonal variations, model differences were the largest in summer.

In comparison, TEMIR and ZHANG, photosynthesis-based and Jarvis-style, respectively, are both governed mainly by solar radiation (see higher G_{sun} in Fig. 4), showing close agreement, except in summer, at the forest sites (ZHANG values are very low). Only these two show a midday depression in G_{sun} at the peak of solar radiation at Mt Kenya (the site with the highest radiation). The ZHANG model also estimated this feature for G_{sun} and G_{st} at other grassland sites (Fig. 3 and 4). This feature could be due to the day length (seasonality) scaling of V_{Cmax} in TEMIR, causing G_{st} to increase significantly during summer at higher latitude sites. In contrast, at lower latitude sites (Mt Kenya and Huancayo, Peru), the seasonal variation in day length is smaller and subsequently smaller seasonality in V_{Cmax} and G_{st}. The TEMIR and the CMAQ_P models, both photosynthesis-based, estimate very similar G_{sun} values (Fig. 4) at PhaDin (fall, winter), IT-Cpz (spring, summer) and FI-Hyy (summer) whereas the G_{st} estimates show significant differences. The opposite occurs at Quabbin where the G_{sun} values of the two models differ much more than the G_{st} estimates. These results illustrate that the different fractionations between shaded and sunlit leaves could mainly contribute to the model spread in stomatal conductance.

Further examination of individual models' features can shed light on the causes of model/site differences in G_{st}. The MESSy G_{st} value is strongly governed by LAI followed by soil moisture, and in all other respects MESSy treats different land cover types the same. Therefore, MESSy simulates the highest G_{st} values at PhaDin, Grignion and Mt. Kenya with LAI values of 6.9, 4.3 and 4.2 $m^2\,m^{-2}$, respectively (Table 1). In contrast to PhaDin, the high LAI site IT-Cpz (6.9 $m^2\,m^{-2}$) experiences significant water stress during summer. This is only captured by MESSy and NOAH indicating higher sensitivity to water stress. During the day, an evident midday depression of G_{st} due to hot weather and water shortage is seen accompanied by a peak in the early morning evident from NOAH, same as has been observed in Mediterranean ecosystems (e.g. Gerosa et al. 2005). The NOAH model accounts for the direct effect of relative humidity on G_{st} (see model description in the supplement) and subsequently modelled a depression in G_{st} at the daily onset (8 am). This variation explains the G_{st} peak at IT-Cpz and Quabbin, which are especially in the summer the two driest among all sites. Due to the dry conditions at the Quabbin site, low soil water and relative humidity, most models, except NOAH, simulate the lowest summer daily mean G_{st} values among all sites. The high estimate by the NOAH model can be explained by the highest V_{Cmax} value among the photosynthesis models (Table 4). The high g_{max} value of 0.55 cm s^{-1} used in

Web-DO_3SE leading to large estimates is largely dampened by strong soil moisture stress at IT-Cpz (Table S2). Similarly, Web-DO_3SE estimates the lowest G_{st} (among the models) values at the Peru site (grassland) due to a strong limitation by the f_{temp} function on stomatal conductance suggesting that the minimum temperature for stomatal opening at 12 °C is too low for these cool temperate conditions. The ZHANG estimates are generally governed by g_{max}, explaining the highest and lowest G_{st} values of all models simulated with the ZHANG model at grassland and forest sites, respectively. The CMAQ_J model has the lowest g_{max} values, but it is strongly impacted by soil moisture. The additional dependence of the ZHANG model on solar radiation is reflected in higher G_{sun} relative to G_{st} (Fig. 3 and 4). TEMIR also simulates the smallest spread of G_{st} among the 3 grassland sites (Ambred, MKenya, Peru), as temperature acclimation of photosynthesis (Kattage and Knorr, 2007) is implemented. The different temperatures among the 3 sites have smaller effects on photosynthetic capacity and G_{st} than other models. Despite explicitly considering soil water stress, TEMIR does not capture the impacts of water stress on G_{st} in IT-Cpz and Quabbin in the summer, as the equivalent soil moisture threshold to trigger soil water stress at IT-Cpz and Quabbin is very low (<0.1 m^3 m^{-3}). Both versions of CMAQ respond very strongly to soil moisture which may not be accurate for each site. The differences between CMAQ-J and CMAQ-P are greatest at the sites with the greatest LAI, such as IT-Cpz and PhaDin.

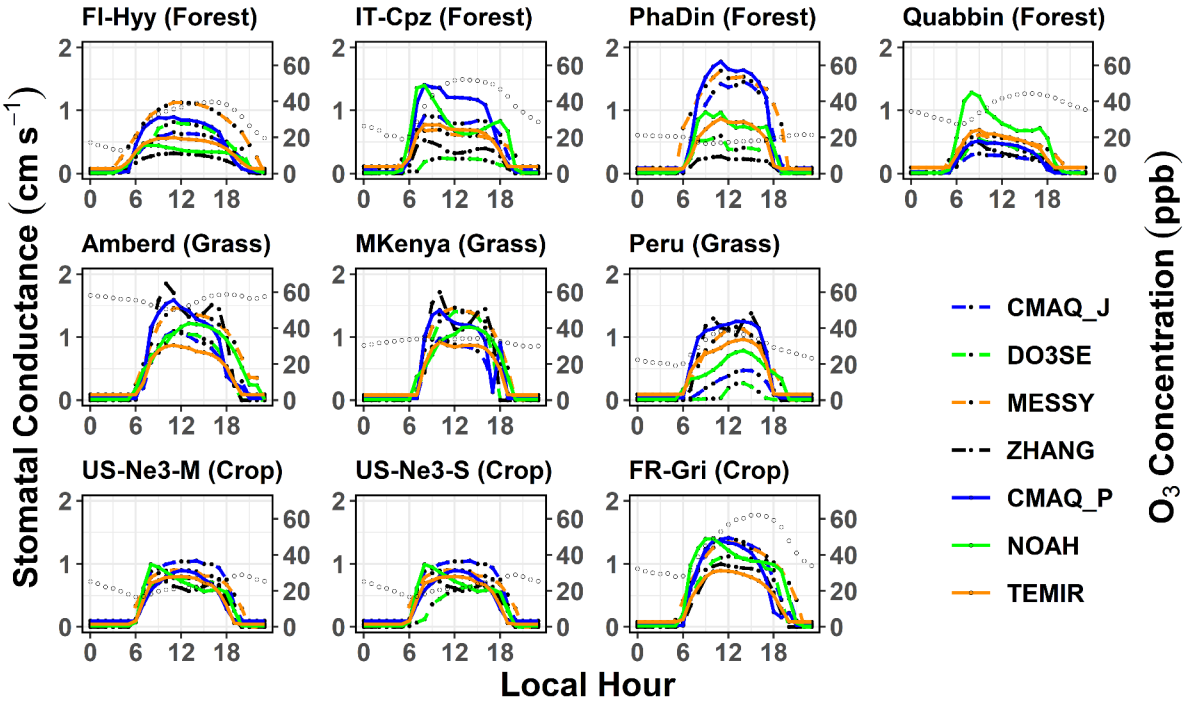

398

399 **Fig. 3 Mean diurnal cycle of total stomatal conductance (G_{st}) from models across various sites during the**
400 **summer season (US-Ne3-S=soybeans, US-Ne3-M=maize). Open circles indicate diurnal O_3 variations.**
401 **Respective figures for the other seasons are presented in the supplement.**

402

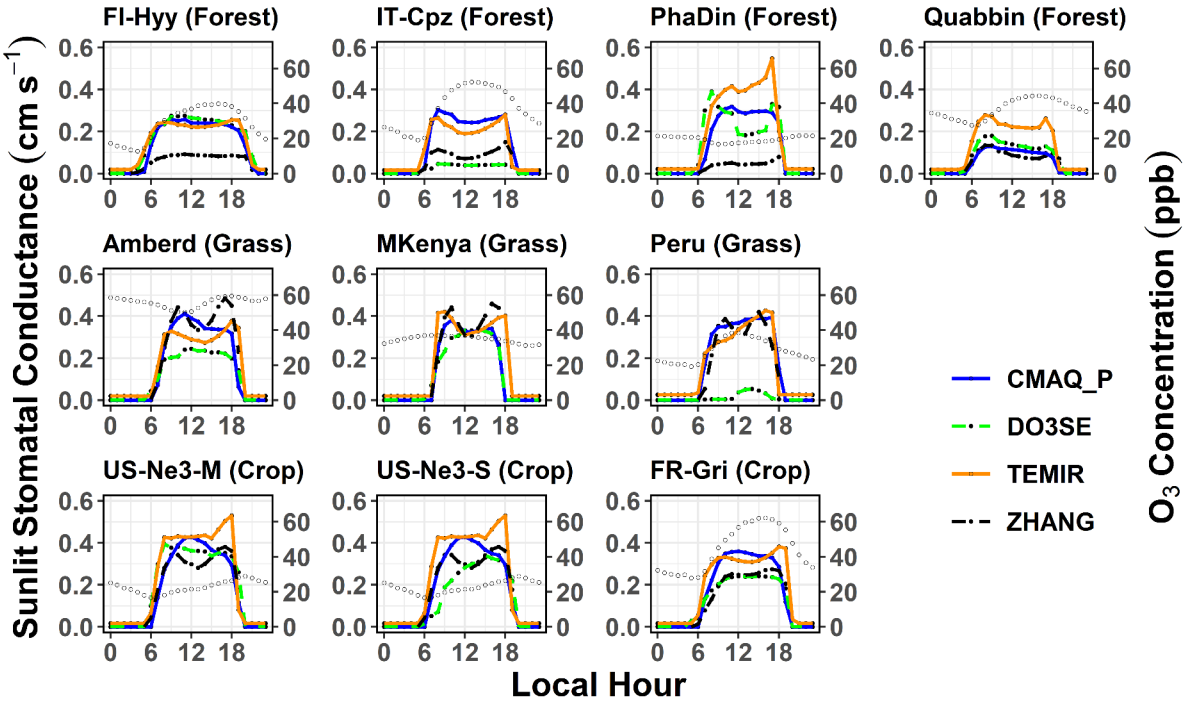

403

404 **Fig 4 Mean diurnal cycle of leaf level sunlit stomatal conductance (G_{sun}) from the 3 two-leaf models**
405 **(CMAQ_P, TEMIR, and ZHANG) across various sites during the summer season (US-Ne3-S=soybeans,**
406 **US-Ne3-M=maize). Open circles indicate diurnal O_3 variations. Respective figures for the other seasons**
407 **are presented in the supplement.**

408

409 The difference between total and sunlit stomatal flux is examined, and trends of stomatal sunlit flux are
410 characterized by different land cover types and climate conditions. Figures 5 and 6 show the (SRAD>50 Wm^{-2})
411 stomatal O_3 flux (F_{st}) and stomatal, sunlit O_3 flux ($F_{st,sun}$) for different models per season at 9 sites representing
412 forest (top), grass (middle), crops (bottom). Thereby, we consider whether G_{st} and O_3 concentration co-variate at
413 diurnal and seasonal timescales. Across all land cover types, a large range of F_{st} (0.05-2 ppb m s^{-1}, Fig. 5) is
414 estimated, usually highest in spring and summer and lowest in winter. The largest median of F_{st} is found at
415 Amberd (0.75 ppb m s^{-1}; ZHANG, summer), followed by IT-Cpz (0.60 ppb m s^{-1}; NOAH, spring), and FR-Gri
416 (0.60 ppb m s^{-1}; MESSy and NOAH, summer) owing to both higher G_{st} and O_3 concentrations at the respective

49
50

sites (Fig. 3). Consequently, no general trend can be identified among the sites, i.e flux estimates can differ within one land cover type. Namely, the two crop sites show very different F_{st} estimates (Fig. 5) since they have the most different O_3 levels across one land cover type. While the FR-Gri site is exposed to an annual mean O_3 of 45 ppb (Table S1) as the lowest O_3 level of 25 ppb among all sites. The same applies for the diurnal variation of O_3 causing either a high (FR-Gri) or a low range (US-Ne3) of flux estimates among all models (in summer and spring). The difference is less apparent in the $F_{st,sun}$ estimates (Fig. 6) which point to the sensitivity of the two leaves to O_3 concentration. Similarly, as seen for the stomatal conductance, three of four models show a very good agreement of F_{st} and $F_{st,sun}$ among each other. In terms of seasonality, models agree also generally well among the grassland sites. Among those (and all land cover types), the maximum annual median $F_{st,sun}$ was estimated for Amberd attributed to the high daytime (7 am - 7 pm) annual O_3 concentrations (49.3 ppb, Table S1). The most different $F_{st,sun}$ (and $F_{st,sun}$) values are found between the ZHANG (highest) and Web-DO$_3$SE model (lowest) due to the difference in G_{sun} (Fig. 4). Web-DO$_3$SE disagrees the most with the other models and predicts very small fluxes at the Peru site following the small G_{st} and G_{sun} values (Fig. 3 and 4).

Among forest sites, spring $F_{st,sun}$ values are comparably high as summer fluxes following the seasonal variation of G_{sun} (Fig. 6, outside the tropics). The highest spring estimates at PhaDin and Quabbin (forests) are linked to the site-specific yearly O_3 maximum in this season (Fig. 3). The flux seasonal maximum is more pronounced in all four models (ZHANG, CMAQ_P, TEMIR) when the O_3 concentration variation during the year is larger at the respective site. The highest $F_{st,sun}$ (0.1 ppb m s^{-1}) is estimated by TEMIR at PhaDin (spring) reflecting the high G_{sun} estimate. In contrast, when considering the total F_{st}, CMAQ_P shows the highest estimate (Fig. 5) which indicates that TEMIR uses a higher sunlit fraction than CMAQ_P as it has been shown for stomatal conductance (Fig. 3 and 4). The difference is most apparent at high LAI sites (PhaDin, IT-Cpz, FR-Gri). The lowest estimates of $F_{st,sun}$ (and a very small spread) at the forest sites are shown by the ZHANG model as it has been explained for G_{st} and G_{sun}. Overall, CMAQ_P has the lowest spread among the models which was also found in the multi-model comparison study by Clifton et al. (2023).

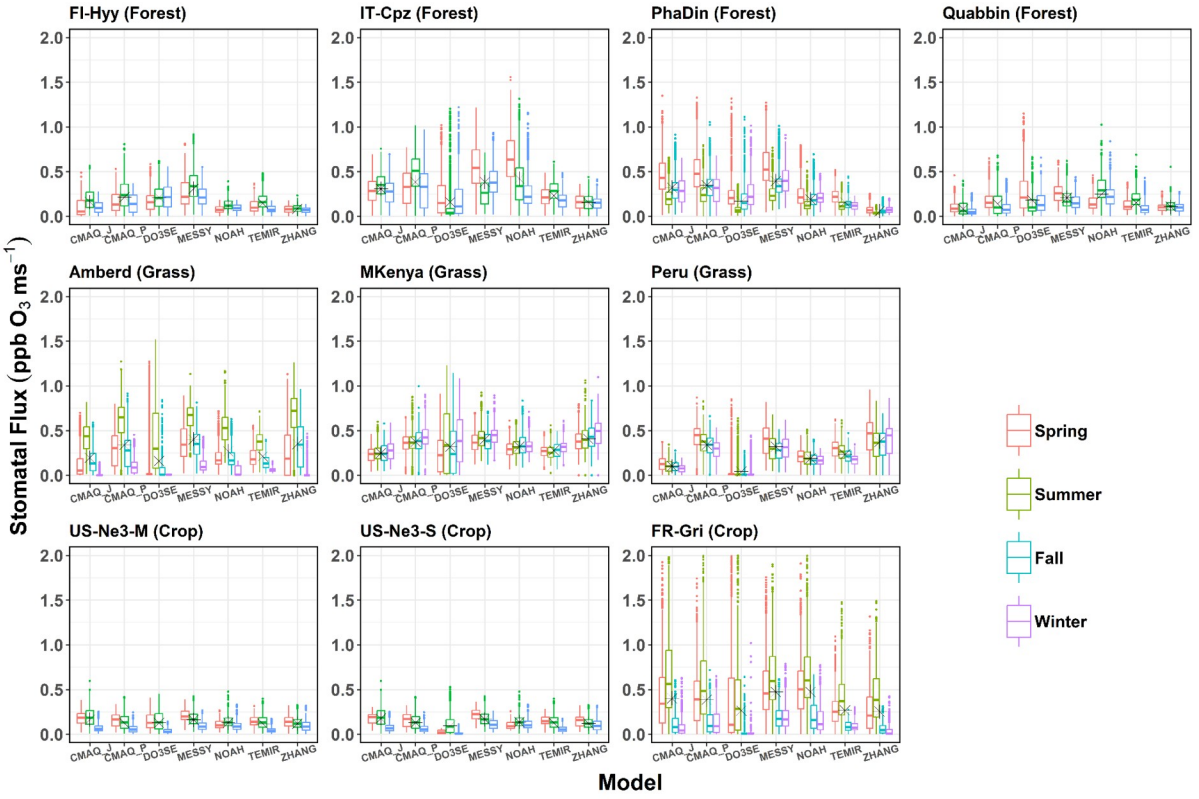

Fig 5: Boxplots of seasonal mean canopy-level total stomatal O_3 flux (ppb ms^{-1}) for different models across various sites (data represent SRAD > 50 W m^{-2} and the growing period).

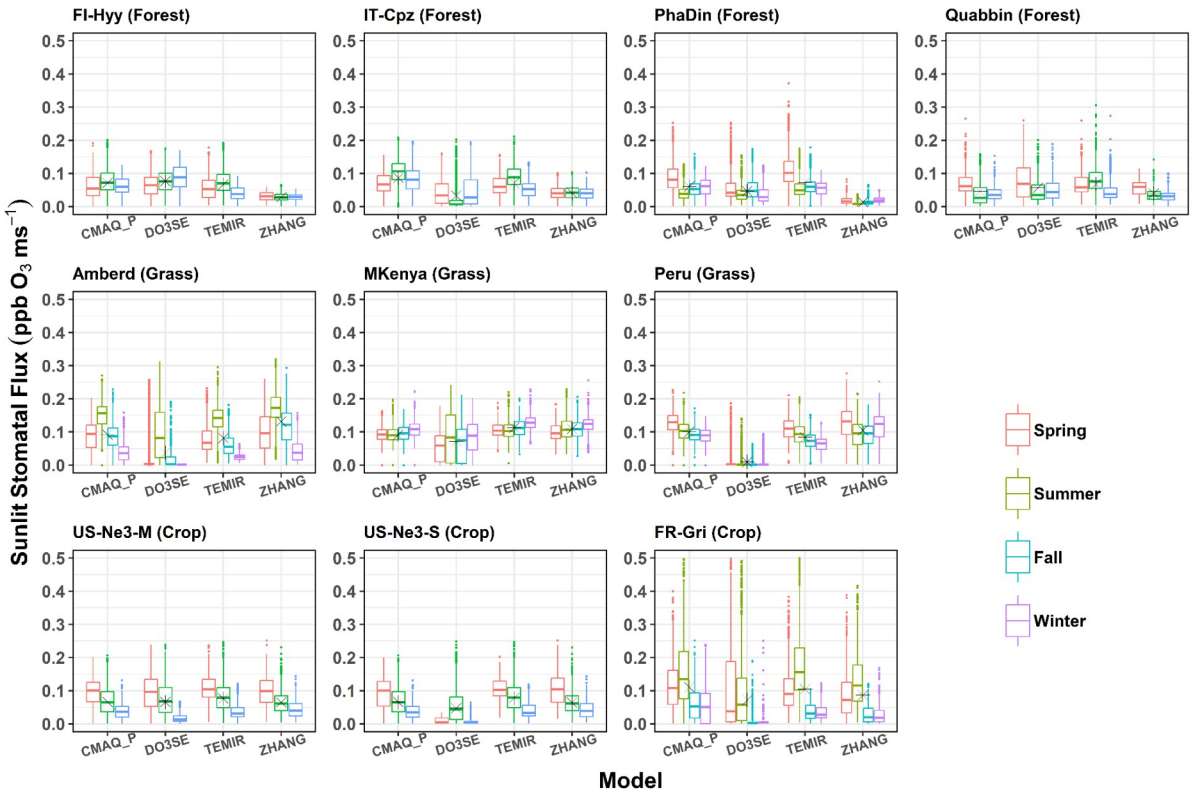

Fig 6: Boxplots of seasonal mean leaf-level sunlit stomatal O_3 flux (ppb ms^{-1}) for different models across various sites (data represent SRAD > 50 W m^{-2} and the growing period).

3.2 Vegetation impact and variation with key input data

This section presents the POD_y calculated from the O_3 deposition by different models at 9 different stations to identify trends and patterns of POD_y among land cover types and climates (Fig. 7, corresponding data in Table S9). The critical threshold for ozone damage y differs for the three land cover types. For forests and grass the y value is 1 nmol O_3 m^{-2} s^{-1} (POD_1) while O3 damage to crops is assumed to occur only when the y threshold exceeds 6 nmol O_3 m^{-2} s^{-1} (POD_6). By driving the models with changed input data of O_3, soil moisture, temperature, relative humidity, growing season (Fig. 8) and with changed Vc_{max}/g_{max} parameter (Fig. 9) we explore the sensitivity of the POD_y estimates. As shown in the previous analysis, the largest O_3 uptake and thus

457 the highest POD_y of 28 mmol O_3 m^{-2} (on average among all models) is estimated over grassland sites (compared
458 to forest and crops) (Fig. 7). POD_1 increases linearly with time for evergreen grasslands whereas Mt. Kenya
459 shows the fastest accumulation (due to the highest F_{st} in spring and summer). Three of the four models lie in a
460 range of 5 mmol O_3 m^{-2} whereas Web-DO$_3$SE predicts a maximum POD_y of 10 mmol O_3 m^{-2} at all grassland
461 sites. Only at the Peru site, these low values can be reasoned by the significantly lower G_{sun} and $F_{st,sun}$ (compared
462 to other models).

463 For forests, our modelled ensemble POD_1 median and maximum values (ranging between 8 and 25 mmol O_3 m^{-2}) are similar in scale to values estimated across broad geographical regions by other studies. Karlsson et al.
465 estimated POD_1 values across Europe with the highest values in mid-latitude Europe for coniferous (15 to 20
466 mmol O_3 m^{-2}) and broadleaf (22 to 28 mmol O_3 m^{-2}) forests. However, the ZHANG and the Web-DO$_3$SE model
467 are estimated to be significantly lower POD_1 than CMAQ_P and TEMIR at each site. These estimates average to
468 16 mmol O_3 m^{-2}. There is no obvious pattern to which models tend to estimate higher or lower POD_1 values, but
469 these estimates are generally consistent with G_{sun} (Fig. 4) and $F_{st,sun}$ (Fig. 6) model estimates explained by
470 particular model constructs or parameterisations. For instance, the ZHANG model estimates low stomatal
471 deposition and thus also POD_y over all forests. Web-DO$_3$SE saw a low O_3 uptake only due to the site conditions
472 at IT-Cpz.

473 For crops, the model estimates of POD_6 are a little more consistent, with modelled differences within sites only
474 varying between ~ 3 and 11 mmol O_3 m^{-2}, however, this could in part be due to the overall lower POD_6 values
475 due to the use of the higher y threshold. Median model ensemble values range between ~7 and 12 mmol O_3 m^{-2}
476 across sites. POD_6 for staple crops has been estimated in other studies across Europe and globally. A European
477 study (Schucht et al., 2020) on wheat found POD_6 values up to ~ 4 mmol O_3 m^{-2} suggesting that our POD_6 values
478 for the FR-Gri site tend to be too high. Feng et al. (2012) estimated maximum POD_6 values of up to 8 mmol O_3
479 m^{-2} for winter wheat in China though these higher values are likely driven by higher ozone concentrations.
480 Similarly, Wang et al. (2022) also found POD_6 values for maize of up to 8 mmol O_3 m^{-2}. Our models give the
481 largest range in POD_6 estimates for soybeans at the US-Ne3 site (0 to 11 mmol O_3 m^{-2}). A key determinant of the
482 range in POD_y simulated by our models, and also with estimates provided in the literature, is the value chosen
483 for g_{max} (or V_{Cmax} depending on the model construct). For example, the multiplicative g_{sto} models used to derive
484 flux-response relationships (see Table 5) use g_{max} values of 450, 126 and 301 mmol O_3 m^{-2} s^{-1} for wheat, maize
485 and soybeans (UNECE LRTAP, 2017; Peng et al., 2019 and Zhang et al., 2017). By contrast, our modelling uses

a variety of g_{max} values, for example, the Web-DO$_3$SE model uses 450, 305 and 300 mmol O_3 m^{-2} s^{-1} for wheat, maize and soybeans. A further consideration in parameter selection are local conditions, a study by Stella et al., (2013) found a g_{max} value of 296 mmol O_3 m^{-2} s^{-1} was most appropriate to describe wheat g_{sto} at the FR-Gri site. This variation highlights the importance of selecting appropriate model parameterisation for conditions, as well as consistency of parameterisation with models used to develop flux response relationships.

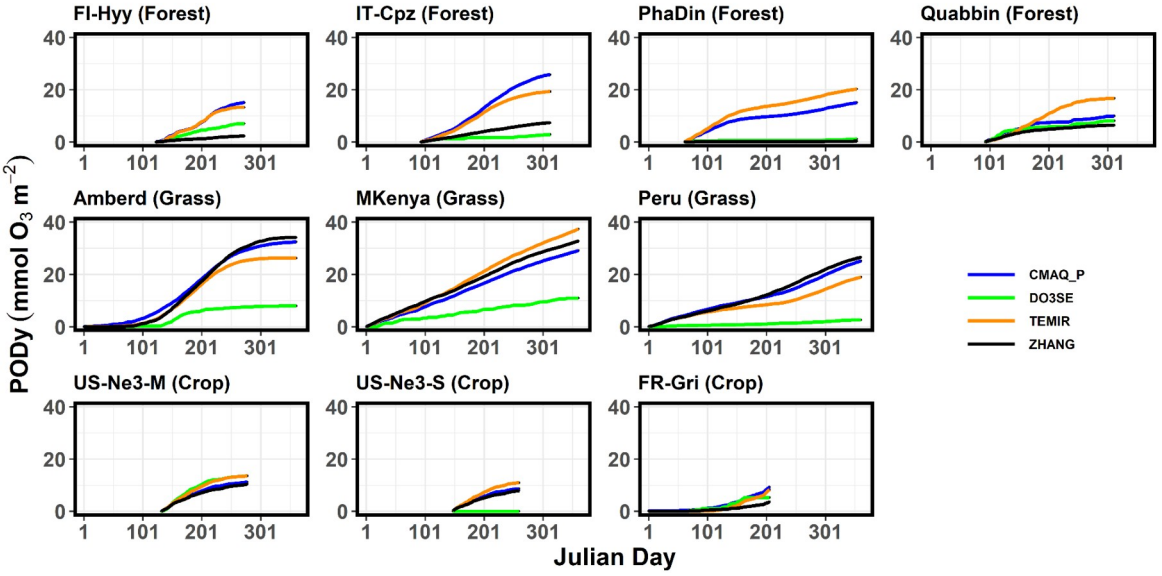

Fig 7: Evolution of POD_y (mmol O_3 m-2) through the growing seasons at various sites.

From the sensitivity analysis, we found that all models show sensitivity of POD_y to changes in O_3, specific humidity, and temperature with varying degrees over different land cover types possibly due to different prescribed values such as the temperature threshold (Fig. 8, corresponding absolute values in Table S10). Especially, the POD_y at all sites is most significantly changed when modifying the O_3 concentration by +-40 % (Table S11). Crop is the most sensitive land cover to O_3 changes across the different models (8.5 mmol m^{-2}; 76 % POD_y change with respect to the base run), followed by forest (10.0 mmol O_3 m^{-2} ; 59.3%) and grass (14.9 mmol O_3 m^{-2}; 56.1%) which is due to the plant physiognomy (Grulke and Heald et al. ,2020). In a relative sense, the average response change in POD_y to a 40 % change in O_3 concentrations is the greatest in ZHANG (+9.2 mmol O_3 m^{-2}, corresponding to a 68.1 % POD_y change with respect to the base run), followed by CMAQ_P and

TEMIR (12 and 11.9 mmol O_3 m^{-2} ;64.8 % and 63.5 %), and then by Web-DO_3SE (11.4 mmol O_3 m^{-2}; 53.0 %). Also, the POD_y estimate seems to be sensitive to humidity (Q) changes (+-30%) among all models. At forest, the POD_y estimates appear to be the most sensitive (4.6 mmol O_3 m^{-2}; 27.3%), followed by crops (2.9 mmol O_3 m^{-2}; 25.9%) and grass (4.6 mmol O_3 m^{-2}; 17.3 %). The response is the greatest in TEMIR and CMAQ (between 5.7 and 6.7 mmol O_3 m^{-2}; 30.7-35.8 %), while it is much smaller for ZHANG (usually close to zero on average). The most non-linear response was shown by Web-DO_3SE at IT-Cpz which estimated a 5 times higher POD_y response to increasing humidity than to a humidity decrease pointing towards the strong dryness at this site limiting If temperature is changed by +-3 K the highest sensitivity was found at crops on average (2.7 mmol O_3 m^{-2}; 24.1%), followed by grass (4.6 mmol O_3 m^{-2}; 17.2 %) and forest (1.6 mmol O_3 m^{-2}; 9.5%). The responses unevenly vary in sign depending on the model because the temperature change depends on the optimal temperature at the specific sites. Namely most models estimate a POD_y decrease when increasing temperature (Fig. 5). As described in Hayes et al. (2019), a temperature increase is seen in southern countries where temperature could limit stomatal uptake since temperature is already close to the optimum in normal conditions. From our sensitivity analysis, temperature impacts on POD_y are noticeable only for a few sites (e.g., Ambered, Mt. Kenya, and Peru) and models's response to POD_y change were different due to different thresholds used for the temperature stress factors to stomatal conductance. The greatest changes in magnitude are predicted by Web-DO_3SE (5.1 mmol O_3 m^{-2}; 23.7%), followed by CMAQ_P (3.1 mmol O_3 m^{-2}; 16.7%), ZHANG (1.9 mmol O_3 m^{-2}; 14.1 %) and TEMIR (1.7 mmol O_3 m^{-2}; 9.6 %). In contrast, not all models are sensitive to changes of soil water content (SWC). The greatest response is seen in CMAQ_P (-6.3 and +1.4 mmol m^{-2}; -34.0% and +7.6%), followed by Web-DO_3SE (-2.2 and -2.2 mmol O_3 m^{-2}; -10.2% and -10.2%), and TEMIR (-1.1 and +0.8 mmol O_3 m^{-2} ; -5.9% and +4.3%), while ZHANG shows no difference in this regard because it is not sensitive to soil moisture. The changes are largest at crops (1.5 mmol O_3 m^{-2}; 13.4%), while grass and forest show similar responses (2.8 and 1.7 mmol O_3 m^{-2}; 10.5 and 10.1 %, respectively). That is in line with De Marco et al. (2020) who show that POD_y responses to soil water changes increase with higher Y threshold (here crops). The models do not appear to be sensitive to LAI 14d shifts, with the only exception of Web-DO_3SE, which simulates a lower POD_y for both early and late LAI shifts (-2.6 mmol O_3 m^{-2} on average, across all land covers). LAI is used as a proxy for growing seasons in most models whereasWeb-DO_3SE considers growing seasons directly.

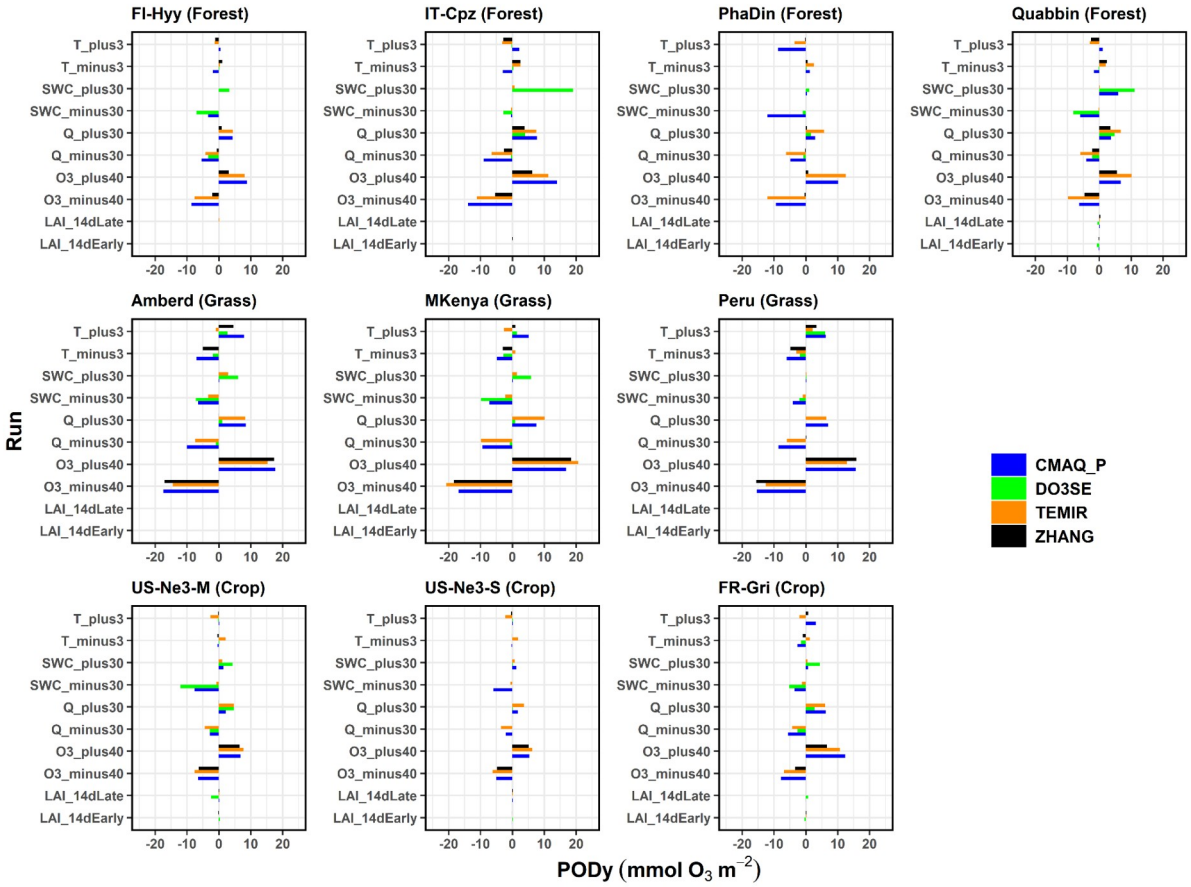

528

529 **Fig 8: Meteorology sensitivity assessment: Absolute change of POD_y values with respect to Base run POD_y**
530 **due to 10 or 20 % variation of the temperature (T), soil water content (SWC), absolute humidity (Q), O_3**
531 **and LAI/growing season.**

532

533 A 20% change of g_{max}/Vc_{max} leads to corresponding changes in POD_y values. An increase or decrease of the
534 parameter leads to very similar changes (in +-) (Fig. 9, corresponding data in Table S12 – S14). The response
535 appears to be generally uniform across sites. On average, the results show +28.9 ± 22.4 % POD_y change for the
536 20 % increase of g_{max}/Vc_{max}, and -27.4 ± 13.1 % for the 20 % decrease with the largest absolute changes at
537 grassland (up to 8 mmol O_3 m^{-2} , ZHANG). At forests and crops, changes up to 5 and 3 mmol O_3 m^{-2} occur,

respectively. Among all sites, noticeably higher (the highest) relative changes were estimated at FR-Gri which thus constituted the only relevant source of variability. This change is significantly different to the change at US-Ne3 (20-30 %) which reflects the contrasting low O_3 level at US-Ne3 compared to the highly polluted FR-Gri site. Also, the ZHANG model predicts the highest changes at crops while CMAQ_P seems insensitive. The ZHANG (and TEMIR) model appears to be the most sensitive model to the changes at most sites due to the strong dependency on the g_{max}/Vc_{max} parameter (see analysis above). The only climate trend of the response is seen by the ZHANG model which shows an average 65 % increase/decrease in wet forests (PhaDin, FI-Hyy) and only a 40 % change in dry places. Sites with very low estimates (PhaDin in ZHANG, Peru in Web-DO_3SE) were excluded from this sensitivity study.

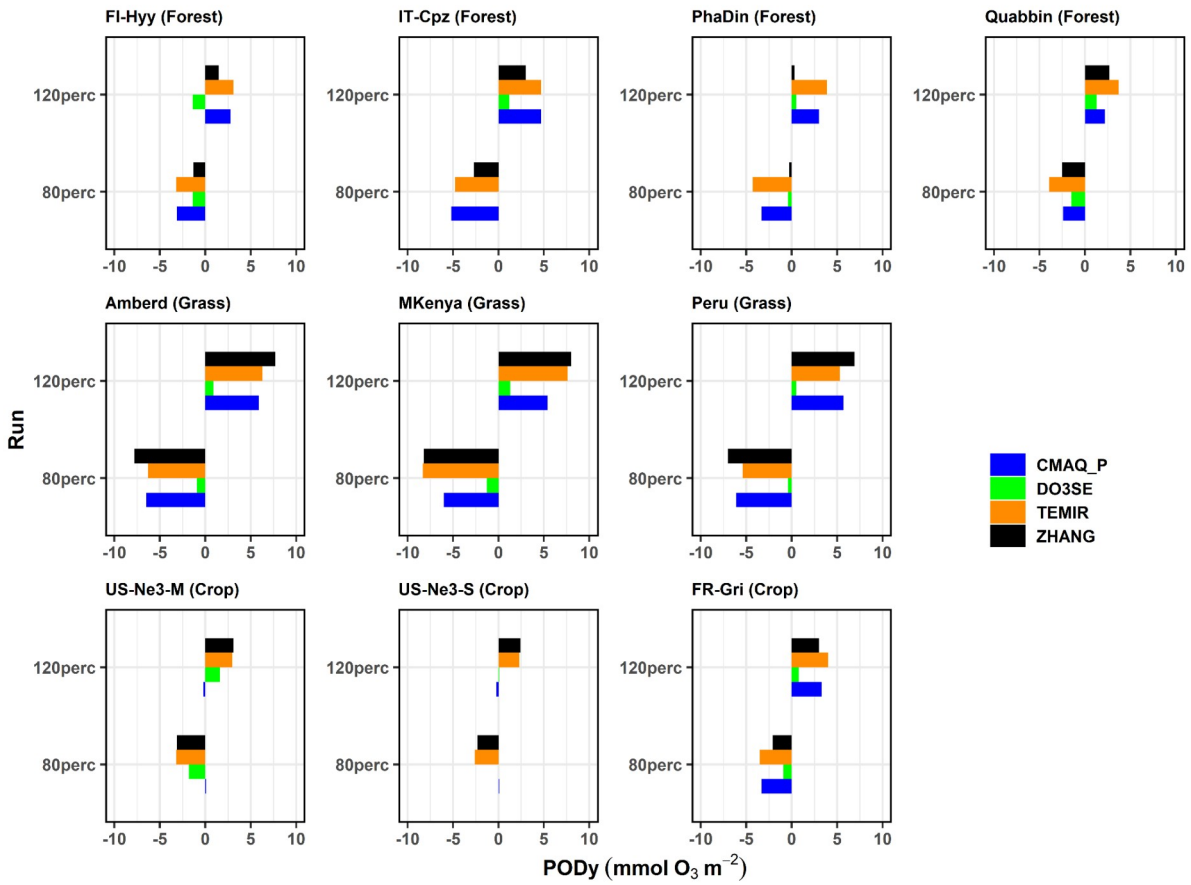

Fig 9: Land cover parameterisation sensitivity assessment: Absolute change of POD_y values with respect to the base run POD_y values due to 20 % variation of G_{max} or V_{Cmax}.

To indicate the likely damage, and range of damage that our modelled values of POD_y predict, we have used POD_y flux-response relationships available in the literature that most closely represent the vegetation type and climatic location of each study site (Table 5). To estimate O_3 damage to forests we use recently derived flux-response relationships that relate POD_1 values to gross annual increment (Karlsson et al., sub) and hence indicate the annual change in growth rate caused by O_3. The mean model ensemble estimates a percentage reduction in gross annual increment of around 5% for FI-Hyy and Pha Din, 6% for IT-Cpz and 14% for Quabbin. However, the range in estimates across models is not insignificant and most extreme at the Quabbin site with a minimum of 11% and a maximum of 21% around the mean 13% value; this is due to broadleaf deciduous species being more sensitive to O_3 dose than needleleaf species and hence more sensitive to a range of POD_y model simulations (Bueker et al., 2015). It should also be emphasised that the Pha Din site uses a European-derived flux-response relationship for an Asian forest site.

563

						PODy			% Response			
Site	**Species**	**y**	**Flux-response relationship**	**Response metric & species**	**min**	**median**	**max**	**min**	**median**	**max**	**Location of PODy relationship**	**Reference**
FI-Hyy	Scots pine	1	y = -0.0057x + 1.0015	Gross Annual Increment (GAI) % for Norway spruce/Scots pine	2.3	10.2	15.1	1.2	5.6	8.5	Europe	Karlsson et al., sub (to TOARII community special issue)
Quabbin	Birch/ Beech (Broadleaf deciduous)	1	y = -0.0093x + 0.9461	Gross Annual Increment (GAI) % for Birch/Beech	6.5	9.1	16.8	11.4	13.9	21.0	Europe	Karlsson et al., sub (to TOARII community special issue)
PhaDin	Norway spruce (Evergreen needleleaf)	1	y = -0.0057x + 1.0015	Gross Annual Increment (GAI) % for Norway spruce/Scots pine	0.4	8.1	20.3	0.0	4.5	11.4	Europe	Karlsson et al., sub (to TOARII community special issue)
IT-Cpz	Holm oak	1	y = -0.0047x + 1.001	Gross Annual Increment (GAI) % for Aleppo pine/Holm Oak	2.8	13.3	25.8	1.2	6.2	12.0	Europe	Karlsson et al., sub (to TOARII community special issue)
FR-Gri	winter wheat	6	y = -0.0385x + 1.003	% grain yield loss for wheat	3.6	6.8	9.3	13.6	25.9	35.5	Europe	UNECE LRTAP Mapping Manual (2017)
US-Ne3 (Maize)	Maize	6	y=0.0426x+1	% grain yield loss for wheat	10.5	12.4	13.6					Peng, J., Shang, B., Xu, Y., Feng, Z., Pleijel, H. and Calatayud, V., 2019. Ozone exposure-and flux-yield response relationships for maize. Environmental pollution, 252, pp.1-7.
US-Ne3 (Soybean)	Soybean	6	y = -0.033x + 1.01	% relative seed yield loss per soybean plant	0.0	8.3	11.0	0.0	26.4	35.3	China	Zhang, W., Feng, Z., Wang, X., Liu, X., Hu, E. (2017) Quantification of ozone exposure- and stomatal uptake-yield response relationships for soybean in Northeast China. Sci of the Total

69 35
70
71

												Env., 599-600 (710-720)
Amber d	Grasslan d	1	y = -0.0062x + 0.947	% total biomass loss for temperate perennial grassland	7.9	29.4	34.1	10.2	23.5	26.4	Europe	UNECE LRTAP Mapping Manual (2017)
MKeny a	Grasslan d	1	y = -0.0062x + 0.947	% total biomass loss for temperate perennial grassland	10.9	31.0	37.4	12.1	24.5	28.5	Europe	UNECE LRTAP Mapping Manual (2017)
Peru	Grasslan d	1	y = -0.0062x + 0.947	% total biomass loss for temperate perennial grassland	2.6	22.1	26.6	6.9	19.0	21.8	Europe	UNECE LRTAP Mapping Manual (2017)

Table 5. Estimates of O_3 damage (for specific response metrics) derived from using the ensemble mean modeled PODy values (and minimum and maximum values) with appropriate flux-response relationships based on land cover type. The climatic location within which the flux-response relationships are derived are stated to show the relevance of their use in estimating damage. Shaded cells denote flux-response relationships that are derived outside of the broad climate region to which they are applied in this study and hence whose damage estimates should be treated with caution.

For crops, flux response relationships are available for wheat, maize and soybeans (UNECE LRTAP, 2917, Peng et al., 2019 and Zhang et al., 2017). These relationships are derived from Europe (wheat) and China (maize and soybean). For wheat, we see a large range in percentage yield loss with a mean model ensemble of 26 % but a maximum yield loss of 35 %. This is driven by high POD_6 values derived from CMAQ_P and TEMIR. For maize at US-Ne3 the results are very consistent with relative grain yield loss estimates ranging from 1.4 to 1.6 %. For soybeans at US-Ne3, the results are less consistent than maize with a minimum and maximum of 0 and 35 % yield around a mean of 26 %. It is important to note that a Chinese-derived flux-response relationship is used to estimate O_3 damage on both US-grown crops.

Finally, for grasslands, we estimate total biomass losses of 19, 24 and 23% from the ensemble model mean for Peru, Mt Kenya and Amberd respectively. The range in model values is relatively small for Amberd and Mt Kenya. A low minimum value of 6 % total biomass loss is estimated for Peru due to the Web-DO$_3$SE model having a very low POD$_y$ at this location due to a likely oversensitive limitation to O_3 uptake caused by low temperatures.

4. Discussion and Conclusion

Here we have compared six deposition schemes commonly used in atmospheric chemistry transport models. We have focussed on the stomatal component of deposition since this is acknowledged to have a substantial influence on damage to vegetation, and ultimately the ability of these six models to estimate the POD$_y$ metric designed to indicate the level of O_3 damage to forest, crops and grasslands. The models estimate POD$_y$ values of 28, 15 and 9 mmol O_3 m^{-2} for grassland, forests and crops, respectively. The multi-model mean estimates are generally in the expected range which suggests that the stomatal flux output of these models could be used for O_3 impact assessments. We also explored the differences in POD$_y$ by geographical location. When comparing one vegetation type, we find multiple drivers including O_3 concentration. The different model types are not the driving force, instead, the models can predict similar results.

There are three key reasons for differences in dry deposition model estimates i. model construct and the inclusion/exclusion of important factors that determine G_{st} and G_{sun}; ii. model parameterisation which may characterise the land cover types and iii. differing model sensitivity to climate variables (seasonal, location effects) in estimates of stomatal deposition. The model comparison of stomatal conductance and stomatal dry deposition for ozone helps us to understand the differences between models. We found that models simulate generally reasonable stomatal deposition of 0.5 -0.8 cm s^{-1} in summer whereas the different model types often agree very well with each other. The stomatal conductance estimates among the models agree with correlation coefficients of 0.75, 0.80 and 0.85 for forests, crops and grasslands. Thereby, the 9 sites selected for this study also reflect different climate conditions; however the selection of sites that provide such broad representations also means that the analysis and the results cannot be generalized. The global coverage, diverse land types and varying meteorological conditions of the 9 sites resulted in widespread model responses to soil moisture (Fig. 8), while appearing to be insensitive to changes of LAI (Fig. 9). The former underscored the idiosyncratic features and hence potential limitations of individual models, whereas the latter gave us confidence in model capabilities despite the different constructs and parameterizations of the models. The model differences, identified during this analysis, can be explained by the model's dependence on the meteorological conditions at sites. Indeed, both model structure (e.g. Raghav, Kumar and Liu 2023) and parameters (Fares et al., 2013) can affect the accuracy of stomatal conductance models. However, studies have shown that when properly calibrated against field observations, structurally different stomatal models can produce similar stomatal

conductance (Fares et al., 2013, Mäkela et al., 2019). Calibrating the key parameters of stomatal conductance models (e.g. g_{max}/Vc_{max}) is a crucial next step to improve the accuracy of stomatal conductance and POD_y estimates, as our sensitivity tests show direct, and possible non-linear relationship between POD_y and g_{max}/Vc_{max} (e.g. at FR-Gri). This is possible with the recent availability of standardised global eddy flux (FLUXNET, Pastorello et al., 2020) and sap flow (SAPFLUXNET, Poyatos et al., 2020) data.

To estimate POD_y for a representative leaf of the upper canopy, the sunlit leaf must be distinguished from the total leaf. Since the effects-based community recognised that sunlit leaves contribute most to carbon assimilation throughout the growing season or O_3-sensitive period (e.g. in wheat, this is considered to be the time from anthesis to maturity) and hence it will better represent damaging O_3 uptake. All flux response relationships for POD_y are developed for such a representative leaf. This is an important distinction since previous model comparison studies (e.g.Clifton et al., 2023) have tended to focus on whole canopy dynamics. These are important to estimate accurately, but to estimate POD_y requires additional canopy level processes, which need i. O_3 concentration at the top of the canopy, ii. wind speed at the top of the canopy and iii. G_{sun} of a representative leaf at the top of the canopy. Studies (Emberson 2020 and references therein) have established thresholds for different land cover types which are used to provide y values for the selected sites with specific land cover types in this study. Some studies suggest that the y threshold for land cover types may vary by global region (e.g. a number of studies suggest higher y values of up to 12 nmol O_3 m^2 s^{-1} is more appropriate for crops and forest tree species in Asia). In this study, which focuses on comparing across models, we maintain consistency and use common y threshold values for each land cover type. However, this is an aspect that would benefit from further study in the future since estimating PODy values with higher thresholds is more challenging for all types of model given the less frequent occurrences of such high O_3 doses.

Our models estimate 30-50 % of stomatal O_3 deposition at sunlit leaves. Thereby, the model estimates of the total stomatal flux are more widespread (during one season) than the estimates of the sunlit only which suggests an important role of the model's partitioning in two big leaves. When calculating POD_y model means estimates generally agree with the literature but most discrepancies between model estimates of POD_y ultimately come down to the differences in simulations of stomatal conductance. The sensitivity analysis of POD_y yields ozone as the most important input variable, to whose changes all models respond similarly. Considering all models and sites together, POD_y were affected most by the O_3 concentration (+-60-80 % site-dependent, i.e., higher O_3 concentration leads to higher POD_y), followed by humidity (30-50 % site-dependent impact). Soil moisture impacts were also significant for the CMAQ_P and Web-DO_3SE model (up to +-68 % and 22 % change). The sensitivity to temperature changes varies strongly among the model and its parametrization. As the plant canopy acts as a persistent sink of O_3, there is a significant vertical gradient of O_3 within the atmospheric surface layer. For example, Travis et al. (2019) show that the midday O_3 concentration at 65 m above ground (mid-point of a first vertical layer of GEOS-Chem v9-02) is 3 ppb higher than the O_3 concentration at 10 m above ground (inferred by Monin-Obukhov Similarity Theory, MOST) over the Southeastern United States. A mismatch between O_3 measurement height and canopy

height can lead to inaccurate POD_y calculation (Gerosa et al, 2017). An O3 bias of 2 ppb as estimated by e.g. Tarasick et al. (2018) would lead to a change of 6-7 % in POD1 (Gerosa et al., 2017). Similarly, we show that the errors in O_3 concentrations propagate non-linearly to POD_y (i.e. 40% changes in O_3 leads to 53 - 68 % changes in POD_y), such a mismatch should be carefully avoided by applying atmospheric surface layer theories (e.g. MOST) to estimate the vertical profile of O_3, and therefore the canopy-top O_3 concentration, if direct measurement or model output of O_3 at canopy top is not available.

Finally, we use flux-response relationships for temperate deciduous (Beech/birch), temperate needleleaf (Norway spruce (*Picea abies*)), crops (wheat (*Triticum aestivum)*, maize (*Zea mays*) and soybeans (*Glycine max*)) and grassland (*Lolium perenne*) to give a suggest the potential likely variation of damage estimates by land cover type and climatic region. These relationships have predominantly been developed for European and Asia forest and crop species. Therefore, they should be applied to other climate regions with caution although recent evidence suggests that tropical forest species may have similar sensitivity to O_3 as European species (Cheeseman et al. 2024). Although there is rather large variability in POD_y values estimated by the model, the median values are relatively robust. Unfortunately, there is only statistical or modelled evidence of actual O_3 damage, and only at a few of the sites investigated. Modelled evidence uses stomatal ozone flux models similar to those used in this study, but which have been parameterised for local site conditions (Stella et al., 2013 for FR-Gri wheat). Simulations with a terrestrial biosphere model suggested an average long-term O_3 inhibition of 10.4% for the period 1992–2011 at the Harvard site (Yue et al 2016); this compares to our model ensemble estimate of 14% GAI biomass loss for Quabbin. A significant but small NEP reduction was found during Spring in the Italian Castelporziano forest site (up to -1.37 %) but not at the FI-Hyy or FR-Gri sites (Savi et al., 2020). Our modelling estimated substantially lower POD_y values and associated damage at Hyy and IT-Cpz than Quabbin though we would expect to see a more substantial O_3 effect than that demonstrated by the NEP statistical modelling (i.e. 5 and 6% GAI biomass loss at FI-Hyy and IT-Cpz respectively). Similar simulations with a different terrestrial biosphere model found only moderate O_3 damage effects (GPP reductions of 4–6 %; Yue & Unger, 2014). This result is driven by low ambient ozone concentrations but also by the choice of a C4 photosynthetic mechanism to estimate stomatal conductance which gives relatively high-water use efficiency). These simulations also suggested that the US-Ne3 experienced a higher ozone effect on GPP than Harvard which is consistent with our modeling for soybeans (but not maize, generally considered an O_3 tolerant crop species; Mills et al 2011). According to the POD_6 estimates made using a SURFATM model, parameterised for Grignon wheat, POD_6 values of 1.094 mmol O_3 m^{-2} were estimated from 1 April to 1 July 2009 which compared with our range of 3.6 to 9.3; the locally parameterised values gave estimated crop yield losses of 4.2%, compared to our median model ensemble estimates of 25% for the winter wheat. This is most likely due to the lower g_{max} value used in the local parameterisation (296 mmol O_3 m^{-2} s^{-1}). However, no

recording of actual damage is given at the FR-Gri site, so it is not possible to tell which of these simulated damage estimates is closer to reality.

The experiments performed here with varying climate and vegetation input data also find a similar sensitivity of POD_y to O_3. It is helpful to have a range of models and model constructs in deposition schemes especially where these have been developed for particular land cover types. When used in damage estimates it is important to ensure that key stressors are included which may be important for that respective geographical region (such as soil and vapour pressure deficit). Recognising that several deposition schemes would be able to reliably predict POD_y for different climates and cover types once they have been parameterised appropriately will extend the usefulness of flux-response relationships.

Overall, this study has demonstrated the widespread applicability and consensus among various numerical stomatal flux methods. Both semi-mechanistic as well as empirical models can generally represent observed ozone fluxes among different land cover types and climates. We identified the key model constructs and parameterisations that cause differences in POD_y estimates. However, none of the models clearly shows a superior overall performance. Instead, all models can be effectively applied, each with its own strengths and weaknesses. Our findings present exciting opportunities to extend applications beyond specific sites and growing seasons, enabling comprehensive global stomatal flux studies over longer periods. Integrating the TOAR database with the Web-DO_3SE model enables automatic model runs for ozone-vegetation impact assessment at a large range of sites using the TOAR database.

Author contributions

T.E.: site selection, TOAR data extraction, data preparation, model support, modelling Web-DO_3SE, writing, coordination. A.M.: modelling (ZHANG, MESSy, NOAH-GEM, TEMIR model), statistics, plots and analysis. L.E.: concept, writing. H.M.: writing, reviewing. L.Z.: concept and writing. L.R: modelling with CMAQ, FLUXNET data preparation. C.B.: debugging and test simulations of Web-DO3SE. A.W.: site selection, preparation of FLUXNET and sensitivity data. G.K.: site selection, TOAR data extraction. G.G.: site analysis. M.H.: plots and reviewing. P.G.: PODy analysis.

Competing interests

The authors have no competing interests.

Acknowledgements

We acknowledge the TOAR team supports the data extraction. The authors acknowledge the access to the meteorological data on the Jülich MeteoCloud provided by Jülich Supercomputing Centre (Krause et al., 2018). We thank the responsible

people of the selected measurement sites for their support in obtaining site information. We greatly appreciate helpful discussions in the earlier stages of the project from the following people: Owen Cooper, Zhaozhong Feng, Laurens Ganzeveld, Meiyun Lin, Martin Schultz, Eran Tas, and Oliver Wild.

Code availability

The Web-DO_3SE source code is freely available at https://toar-data.fz-juelich.de/ under the CC-BY 4.0 license (https://creativecommons.org/licenses/by/4.0/). The further model code can be obtained upon request.

Data availability

The TOAR data is freely available at https://toar-data.fz-juelich.de/ under the CC-BY 4.0 license (https://creativecommons.org/licenses/by/4.0/). The ERA5 data used can be downloaded from the MeteoCloud server (https://datapub.fz-juelich.de/slcs/meteocloud/index.html). FLUXNET 2015 dataset is publicly available at https://fluxnet.org/data/fluxnet2015-dataset/. Stomatal conductance estimates, and the related FLUXNET 2015 data from SynFlux version 2 can be obtained by contacting Christopher Holmes (cdholmes@fsu.edu).

References

Ainsworth, E. A., Yendrek, C. R., Sitch, S., Collins, W. J., and Emberson, L. D.: The effects of tropospheric ozone on net primary productivity and implications for climate change. Annual review of plant biology, 63(1), 637-661, https://doi.org/10.1146/annurev-arplant-042110-103829, 2012.

Ainsworth, E. A.: Understanding and improving global crop response to ozone pollution. The Plant Journal, 90(5), 886-897, https://doi.org/10.1111/tpj.13298, 2017.

Avnery, S., Mauzerall, D. L., Liu, J., and Horowitz, L. W.: Global Crop Yield Reductions due to Surface Ozone Exposure: 1. Year 2000 Crop Production Losses and Economic Damage, Atmos. Environ., 45, 2284–2296, https://doi.org/10.1016/j.atmosenv.2010.11.045, 2011.

Aguilos, M., Hérault, B., Burban, B., Wagner, F., & Bonal, D.: What drives long-term variations in carbon flux and balance in a tropical rainforest in French Guiana?. Agricultural and forest meteorology, 253, 114-123, https://doi.org/10.1016/j.agrformet.2018.02.009, 2018.

Amos, B., Arkebauer, T. J., and Doran, J. W.: Soil surface fluxes of greenhouse gases in an irrigated maize-based agroecosystem. Soil Science Society of America Journal, 69(2), 387-395, https://doi.org/10.2136/sssaj2005.0387, 2015.

Beck, H. E., McVicar, T.R., Vergopolan, N. Berg, A., Lutsko, N. J., Dufour, A., Zeng, Z., Jiang, X., van Dijk, A. I. J. M., and Miralles, D. G.: High-resolution (1 km) Köppen-Geiger maps for 1901–2099 based on constrained CMIP6 projections. Sci Data 10, 724, https://doi.org/10.1038/s41597-023-02549-6, 2023.

Broberg, M. C., Feng, Z., Xin, Y.,and Pleijel, H.: Ozone effects on wheat grain quality–A summary. Environmental Pollution, 197, 203-213, https://doi.org/10.1016/j.envpol.2014.12.009, 2015

Büker, P., Feng, Z., Uddling, J., Briolat, A., Alonso, R., Braun, S., Elvira, S., Gerosa, G., Karlsson, P.E., Le Thiec, D. and Marzuoli, R., 2015.: New flux based dose–response relationships for ozone for European forest tree species. Environmental Pollution, 206, pp.163-174. https://doi.org/10.1016/j.envpol.2015.06.033 , 2015.

Bukowiecki, N., Steinbacher, M., Henne, S., Nguyen, N.A., Nguyen, X.A., Hoang, A.L., Nguyen, D.L., Duong, H.L., Engling, G., Wehrle, G., Gysel-Beer, M. and Baltensperger, U.: Effect of Large-scale Biomass Burning on Aerosol Optical Properties at the GAW Regional Station Pha Din, Vietnam. Aerosol Air Qual. Res. 19: 1172-1187, https://doi.org /10.4209/aaqr.2018.11.0406, 2019.

Clifton, O. E., Fiore, A. M., Munger, J. W., and Wehr, R.: Spatiotemporal controls on observed daytime ozone deposition velocity over northeastern US forests during summer. Journal of Geophysical Research: Atmospheres, 124(10), 5612-5628, https://doi.org /10.1029/2018JD029073, 2019.

Clifton, O. E., D. L. Lombardozzi, A. M. Fiore, F. Paulot, and L. W. Horowitz.: Stomatal conductance influences interannual variability and long-term changes in regional cumulative plant uptake of ozone. Environmental Research Letters. https://doi.org /10.1088/1748-9326/abc3f1, 2020a.

Clifton, O. E., Paulot, F., Fiore, A. M., Horowitz, L. W., Correa, G., Baublitz, C. B., ... and Weng, E.: Influence of dynamic ozone dry deposition on ozone pollution. Journal of Geophysical Research: Atmospheres, 125(8), https://doi.org /10.1029/2020JD032398, 2020b.

Clifton, O. E., Schwede, D., Hogrefe, C., Bash, J. O., Bland, S., Cheung, P., Coyle, M., Emberson, L., Flemming, J., Fredj, E., Galmarini, S., Ganzeveld, L., Gazetas, O., Goded, I., Holmes, C. D., Horváth, L., Huijnen, V., Li, Q., Makar, P. A., Mammarella, I., Manca, G., Munger, J. W., Pérez-Camanyo, J. L., Pleim, J., Ran, L., San Jose, R., Silva, S. J., Staebler, R.,

Sun, S., Tai, A. P. K., Tas, E., Vesala, T., Weidinger, T., Wu, Z., and Zhang, L.: A single-point modeling approach for the intercomparison and evaluation of ozone dry deposition across chemical transport models (Activity 2 of AQMEII4), Atmos. Chem. Phys., 23, 9911–9961, https://doi.org /10.5194/acp-23-9911-2023, 2023.

Chen, X., Quéléver, L. L. J., Fung, P. L., Kesti, J., Rissanen, M. P., Bäck, J., Keronen, P., Junninen, H., Petäjä, T., Kerminen, V.-M., and Kulmala, M.: Observations of ozone depletion events in a Finnish boreal forest, Atmos. Chem. Phys., 18, 49–63, https://doi.org /10.5194/acp-18-49-2018, 2018 .

Copernicus Climate Change Service (C3S) (2017): ERA5: Fifth generation of ECMWF atmospheric reanalyses of the global climate. Copernicus Climate Change Service Climate Data Store (CDS), date of access: 27.11.2024. https://cds.climate.copernicus.eu/cdsapp#!/home

De Marco, A., Anav, A., Sicard, P., Feng, Z., and Paoletti, E.: High spatial resolution ozone risk-assessment for Asian forests. Environmental Research Letters, 15(10), 104095, https://doi.org /10.1088/1748-9326/abb501, 2020.

Ducker, J. A., Holmes, C. D., Keenan, T. F., Fares, S., Goldstein, A. H., Mammarella, I., Munger, J. W. and Schnell, J.: Synthetic ozone deposition and stomatal uptake at flux tower sites. Biogeosciences, *15*(17), 5395-5413, https://doi.org /10.5194/bg-15-5395-2018, 2018.

Emberson, L.: Effects of ozone on agriculture, forests and grasslands. *Philosophical Transactions of the Royal Society A*, *378*(2183), 20190327, https://doi.org /10.1098/rsta.2019.0327, 2020.

Emmerichs, T.; Kerkweg, A.; Ouwersloot, H.; Fares, S.; Mammarella, I.; Taraborrelli, D.: A Revised Dry Deposition Scheme for Land–Atmosphere Exchange of Trace Gases in ECHAM/MESSy v2.54. Geoscientific Model Development, *14* (1), 495–519. https://doi.org /10.5194/gmd-14-495-2021, 2021.

Fares, S., Mereu, S., Scarascia Mugnozza, G., Vitale, M., Manes, F., Frattoni, M., ... and Loreto, F.: The ACCENT-VOCBAS field campaign on biosphere-atmosphere interactions in a Mediterranean ecosystem of Castelporziano (Rome): site characteristics, climatic and meteorological conditions, and eco-physiology of vegetation. Biogeosciences, 6(6), 1043-1058, https://doi.org /10.5194/bg-6-1043-2009, 2009.

Fares, S. Measured and modelled stomatal and non-stomatal ozone fluxes in a mixed Mediterranean forest. In 25th ICP-Vegetation Task Force Meeting. gennaio–2 febbraio 2012, Brescia, Italia.,2012.

Fares, S., Savi, F., Muller, J., Matteucci, G., and Paoletti, E.: Simultaneous measurements of above and below canopy ozone fluxes help partitioning ozone deposition between its various sinks in a Mediterranean Oak Forest. Agricultural and Forest Meteorology, 198, 181-191. https://doi.org /10.1016/j.agrformet.2014.08.014, 2014.

Fares, S., Matteucci, G., Mugnozza, G. S., Morani, A., Calfapietra, C., Salvatori, E., ... and Loreto, F. : Testing of models of stomatal ozone fluxes with field measurements in a mixed Mediterranean forest. Atmospheric environment, 67, 242-251, https://doi.org /10.1016/j.atmosenv.2012.11.007, 2013.

Feng, Z., Tang, H., Uddling, J., Pleijel, H., Kobayashi, K., Zhu, J., ... and Guo, W.: A stomatal ozone flux–response relationship to assess ozone-induced yield loss of winter wheat in subtropical China. Environmental pollution, 164, 16-23. https://doi.org /10.1016/j.envpol.2012.01.014, 2012.

Fowler, D., Flechard, C., Cape, J.N. et al.: Measurements of Ozone Deposition to Vegetation Quantifying the Flux, the Stomatal and Non-Stomatal Components. Water, Air, & Soil Pollution 130, 63–74. https://doi.org /10.1023/A:1012243317471, 2001.

Fuhrer, J., Val Martin, M., Mills, G., Heald, C. L., Harmens, H., Hayes, F., ... and Ashmore, M. R.: Current and future ozone risks to global terrestrial biodiversity and ecosystem processes. Ecology and evolution, 6(24), 8785-8799. https://doi.org /10.1002/ece3.2568, 2016.

Ganzeveld, L., & Lelieveld, J.: Dry deposition parameterization in a chemistry general circulation model and its influence on the distribution of reactive trace gases. Journal of Geophysical Research: Atmospheres, 100(D10), 20999-21012. https://doi.org /10.1029/95JD02266, 1995.

Gerosa, G., Vitale, M., Finco, A., Manes, F., Denti, A. B. and Cieslik, S.: Ozone uptake by an evergreen Mediterranean Forest (Quercus ilex) in Italy. Part I: Micrometeorological flux measurements and flux partitioning. Atmospheric Environment, 39(18), 3255-3266, https://doi.org /10.1016/j.atmosenv.2005.01.056, 2005.

Gerosa, G., Marzuoli, R., Monteleone, B., Chiesa, M., and Finco, A.: Vertical ozone gradients above forests. Comparison of different calculation options with direct ozone measurements above a mature forest and consequences for ozone risk assessment. Forests, 8(9), 337. https://doi.org /10.3390/f8090337, 2017.

Gerosa G., Marzuoli R., Finco A.: Interannual variability of ozone fluxes in a broadleaf deciduous forest in Italy. ELEMENTA: Science of the Anthropocene 10(1), 00105. https://doi.org /10.1525/elementa.2021.00105, 2022.

Guaita P.R., Marzuoli R., Gerosa G.A.: A regional scale flux-based O3 risk assessment for winter wheat in northern Italy, and effects of different spatio-temporal resolutions. Environmental Pollution 333, 121860, https://doi.org 10.1016/j.envpol.2023.121860, 2023.

Hardacre, C., Wild, O., and Emberson, L.: An evaluation of ozone dry deposition in global scale chemistry climate models, Atmos. Chem. Phys., 15, 6419–6436, https://doi.org /10.5194/acp-15-6419-2015, 2015.

Hayes, F., Mills, G., Alonso, R., González-Fernández, I., Coyle, M., Grünhage, L., ... and Marzuoli, R.: A site-specific analysis of the implications of a changing ozone profile and climate for stomatal ozone fluxes in Europe. Water, Air, & Soil Pollution, 230, 1-15, https://doi.org /10.1007/s11270-018-4057-x, 2019.

Henne, S., Junkermann, W., Kariuki, J. M., Aseyo, J. and Klausen, J.: Mount Kenya Global Atmosphere Watch Station (MKN): Installation and Meteorological Characterization. J. Appl. Meteor. Climatol., 47, 2946–2962, https://doi.org /10.1175/2008JAMC1834.1, 2008a.

Henne, S., Klausen, J., Junkermann, W., Kariuki, J. M., Aseyo, J. O., and Buchmann, B.: Representativeness and climatology of carbon monoxide and ozone at the global GAW station Mt. Kenya in equatorial Africa, Atmos. Chem. Phys., 8, 3119–3139, https://doi.org /10.5194/acp-8-3119-2008, 2008b.

Hersbach, H., Bell, B., Berrisford, P., Hirahara, S., Horányi, A., Muñoz-Sabater, J., ... and Thépaut, J. N.: The ERA5 global reanalysis. Quarterly Journal of the Royal Meteorological Society, 146(730), 1999-2049, https://doi.org /10.1002/qj.3803, 2020.

Horváth, L., Koncz, P., Móring, A. et al.: An Attempt to Partition Stomatal and Non-stomatal Ozone Deposition Parts on a Short Grassland. Boundary-Layer Meteorol 167, 303–326, https://doi.org/10.1007/s10546-017-0310-x, 2018.

Huang, M., Crawford, J. H., Carmichael, G. R., Bowman, K. W., Kumar, S. V., and Sweeney, C.: Satellite soil moisture data assimilation impacts on modeling weather variables and ozone in the southeastern US – Part 2: Sensitivity to dry-deposition parameterizations, Atmos. Chem. Phys., 22, 7461–7487, https://doi.org /10.5194/acp-22-7461-2022, 2022.

Jägermeyr, J, Müller, C., Minoli, S., Ray, D., and Siebert., S.: GGCMI Phase 3 crop calendar [Data set]. Zenodo. https://doi.org /10.5281/zenodo.5062513, 2021a.

Jägermeyr et al.: Climate impacts on global agriculture emerge earlier in new generation of climate and crop, Nature Food, 2, 873–885, https://www.nature.com/articles/s43016-021-00400-y, 2021b.

Junninen, H., Lauri, A., Keronen, P., Aalto, P., Hiltunen, V., Hari, P., Kulmala, M. 2009. Smart-SMEAR: online data exploration and visualization tool for SMEAR stations. Boreal Environment Research 14, 447–457, http://www.borenv.net/BER/pdfs/ber14/ber14-447.pdf, 2009.

Grulke, N. E. and Heath, R. L.: Ozone effects on plants in natural ecosystems. Plant Biology, 22, 12-37. https://doi.org/10.1111/plb.12971, 2020.

Khan, A. M., Clifton, O. E., Bash, J. O., Bland, S., Booth, N., Cheung, P., ... and Stoy, P. C.: Ozone dry deposition through plant stomata: Multi-model comparison with flux observations and the role of water stress as part of AQMEII4 Activity 2. EGUsphere, 2024, 1-34. https://doi.org /10.5194/egusphere-2024-3038 , 2024.

Kattge, J. and Knorr, W.: Temperature acclimation in a biochemical model of photosynthesis: a reanalysis of data from 36 species. Plant, cell & environment, 30(9), 1176-1190, https://doi.org /10.1111/j.1365-3040.2007.01690.x, 2007.

Krause, D., & Thörnig, P.: JURECA: modular supercomputer at Jülich supercomputing centre. Journal of large-scale research facilities JLSRF, *4*, A132-A132, https://doi.org /10.17815/jlsrf-4-121-1, 2018.

Li, M., Wu, P., & Ma, Z.: A comprehensive evaluation of soil moisture and soil temperature from third-generation atmospheric and land reanalysis data sets. Int. J. Climatol, 40(13), 5744-5766, https://doi.org /10.1002/joc.6549, 2020.

Leung, F., Williams, K., Sitch, S., Tai, A. P., Wiltshire, A., Gornall, J., ... and Scoby, D.: Calibrating soybean parameters in JULES 5.0 from the US-Ne2/3 FLUXNET sites and the SoyFACE-O< sub> 3</sub> experiment. Geoscientific Model Development, 13(12), 6201-6213, doi: 10.5194/gmd-13-6201-2020, 2020.

Mäkelä, J., Knauer, J., Aurela, M., Black, A., Heimann, M., Kobayashi, H., ... and Aalto, T.: Parameter calibration and stomatal conductance formulation comparison for boreal forests with adaptive population importance sampler in the land surface model JSBACH. Geoscientific Model Development, 12(9), 4075-4098. https://doi.org/10.5194/gmd-12-4075-2019, 2019.

McGrath, J. M., Betzelberger, A. M., Wang, S., Shook, E., Zhu, X. G., Long, S. P., & Ainsworth, E. A.: An analysis of ozone damage to historical maize and soybean yields in the United States. Proceedings of the National Academy of Sciences, *112*(46), 14390-14395, https://doi.org /10.1073/pnas.1509777112, 2015.

Meszaros, R., Horváth, L., Weidinger, T., Neftel, A., Nemitz, E., Dämmgen, U., ... and Loubet, B.: Measurement and modelling ozone fluxes over a cut and fertilized grassland. Biogeosciences, 6(10), 1987-1999. https://doi.org/10.5194/bg-6-1987-2009, 2009.

Meyers, T. P., Finkelstein, P., Clarke, J., Ellestad, T. G., and Sims, P. F.: A multilayer model for inferring dry deposition using standard meteorological measurements. Journal of Geophysical Research: Atmospheres, 103(D17), 22645-22661, https://doi.org/10.1029/98JD01564, 1998.

Mills, G., Hayes, F., Simpson, D., Emberson, L., Norris, D., Harmens, H. and Büker, P., Evidence of widespread effects of ozone on crops and (semi-)natural vegetation in Europe (1990–2006) in relation to AOT40- and flux-based risk maps. Global Change Biology, 17: 592-613, https://doi.org/10.1111/j.1365-2486.2010.02217.x, 2011.

Mills, G., Pleijel, H., Malley, C. S., Sinha, B., Cooper, O. R., Schultz, M. G., Neufeld, H. S., Simpson, D., Sharps, K., Feng, Z., Gerosa, G., Harmens, H., Kobayashi, K., Saxena, P., Paoletti, E., Sinha, V., Xu, X.: Tropospheric Ozone Assessment Report: Present-day tropospheric ozone distribution and trends relevant to vegetation. Elementa: Science of the Anthropocene; 6 47, https://doi.org/10.1525/elementa.302, 2018.

Monks, P. S., Archibald, A. T., Colette, A., Cooper, O., Coyle, M., Derwent, R., ... and Williams, M. L.: Tropospheric ozone and its precursors from the urban to the global scale from air quality to short-lived climate forcer. Atmospheric chemistry and physics, *15*(15), 8889-8973. https://doi.org/10.5194/acp-15-8889-2015, 2015.

Pastorello, G., Trotta, C., Canfora, E.: The FLUXNET2015 dataset and the ONEFlux processing pipeline for eddy covariance data. Sci Data 7, 225, https://doi.org/10.1038/s41597-020-0534-3, 2020.

Pieber, S.M., Henne, S., Nguyen, N.A., Nguyen, DL., Steinbacher, M.: Trace Gases and Air Quality in Northwestern Vietnam During Recurrent Biomass Burning on the Indochina Peninsula Since 2014—Field Observations and Atmospheric Simulations. In: Vadrevu, K.P., Ohara, T., Justice, C. (eds) Vegetation Fires and Pollution in Asia. Springer, Cham. https://doi.org/10.1007/978-3-031-29916-2_32, 2023.

Pleim, J. and Ran, L.: Surface flux modeling for air quality applications. Atmosphere, 2(3), pp.271-302. https://doi.org/10.3390/atmos2030271, 2011.

Poyatos, R., Granda, V., Flo, V., Adams, M. A., Adorján, B., Aguadé, D., ... and Van Der Tol, C.: Global transpiration data from sap flow measurements: the SAPFLUXNET database. Earth System Science Data, 13, 2607–2649, https://doi.org/10.5194/essd-13-2607-2021, 2021.

Putaud J.P., Bergamaschi, P., Bressi, M., Cavalli, F., Cescatti, A., Daou, D., Dell'Acqua, A., Douglas, K., Duerr, M., Fumagalli, I., Goded, I., Grassi, F., Gruening, C., Hjorth, J., Jensen, N. R., Lagler, F., Manca, G., Martins Dos Santos, S., Matteucci, M., , Passarella, R., Pedroni, V., Pokorska, O., Roux, D.: JRC – Ispra Atmosphere - Biosphere - Climate Integrated monitoring Station: 2014 Report; EUR 27639 EN, https://doi.org/10.2788/570407, 2014.

Ran, L., Pleim, J., Song, C., Band, L., Walker, J.T. and Binkowski, F.S.: A photosynthesis-based two-leaf canopy stomatal conductance model for meteorology and air quality modeling with WRF/CMAQ PX LSM. Journal of Geophysical Research: Atmospheres, 122(3), pp.1930-1952, https://doi.org/10.1002/2016JD025583, 2017.

Raghav, P., Kumar, M., and Liu, Y.: Structural constraints in current stomatal conductance models preclude accurate estimation of evapotranspiration and its partitions, https://doi.org/10.1029/2024WR037652, 2023.

Ramya, A., Dhevagi, P., Poornima, R., Avudainayagam, S., Watanabe, M., and Agathokleous, E.: Effect of ozone stress on crop productivity: A threat to food security. *Environmental Research*, 116816. https://doi.org/10.1016/j.envres.2023.116816, 2023.

Savi, F. and Fares, S.: Ozone dynamics in a Mediterranean Holm oak forest: comparison among transition periods characterized by different amounts of precipitation. Annals of Silvicultural Research 38(1) 1-6 http://dx.doi.org/10.12899/ASR-801, 2014

Schröder, S., Schultz, M. G., Selke, N., Sun, J., Ahring, J., Mozaffari, A., Romberg, M., Epp, E., Lensing, M., Apweiler, S., Leufen, L. H., Betancourt, C., Hagemeier, B., Rajveer, S.: TOAR Data Infrastructure, https://doi.org/10.34730/4d9a287dec0b42f1aa6d244de8f19eb3, 2021.

Schucht, S., Tognet, F., Létinois, L. and Ineris, I.N.: Wheat yield loss in 2019 in Europe due to ozone exposure, Eionet Report-ETC/ATNI, 2021.

Silva, S. J. and Heald, C. L.: Investigating dry deposition of ozone to vegetation. Journal of Geophysical Research: Atmospheres, 123(1), 559-573. https://doi.org/10.1002/2017JD027278, 2018.

Stella, Patrick, et al.: Predicting and partitioning ozone fluxes to maize crops from sowing to harvest: the Surfatm-O 3 model, Biogeosciences 8.10, 2869-2886. https://doi.org/10.5194/bg-8-2869-2011, 2011.

Stella, P., Personne, E., Lamaud, E., Loubet, B., Trebs, I., & Cellier, P. (2013). Assessment of the total, stomatal, cuticular, and soil 2 year ozone budgets of an agricultural field with winter wheat and maize crops, Journal of Geophysical Research: Biogeosciences, 118(3), 1120-1132, https://doi.org/10.1002/jgrg.20094, 2013.

Sofen, E. D., Bowdalo, D., Evans, M. J., Apadula, F., Bonasoni, P., Cupeiro, M., ... and Tørseth, K.: Gridded global surface ozone metrics for atmospheric chemistry model evaluation. Earth System Science Data, 8(1), 41-59, https://doi.org/10.5194/essd-8-41-2016, 2016.

Sun, S., Tai, A. P. K., Yung, D. H. Y., Wong, A. Y. H., Ducker, J. A., and Holmes, C. D.: Influence of plant ecophysiology on ozone dry deposition: comparing between multiplicative and photosynthesis-based dry deposition schemes and their responses to rising CO_2 level, Biogeosciences, 19, 1753–1776, https://doi.org/10.5194/bg-19-1753-2022, 2022.

Tai, A. P., Yung, D. H., & Lam, T. : Terrestrial Ecosystem Model in R (TEMIR) version 1.0: simulating ecophysiological responses of vegetation to atmospheric chemical and meteorological changes. Geoscientific Model Development, 17(9), 3733-3764, https://doi.org/10.5194/gmd-17-3733-2024, 2024.

Travis, K. R. and Jacob, D. J.: Systematic bias in evaluating chemical transport models with maximum daily 8 h average (MDA8) surface ozone for air quality applications: a case study with GEOS-Chem v9. 02. Geoscientific Model Development, 12(8), 3641-3648. https://doi.org/10.5194/gmd-12-3641-2019, 2019.

UNECE LRTAP (2017). III. Mapping critical levels for vegetation. Available at: https://icpvegetation.ceh.ac.uk/sites/default/files/FinalnewChapter3v4Oct2017_000.pdf

Visser, A. J., Ganzeveld, L. N., Goded, I., Krol, M. C., Mammarella, I., Manca, G., and Boersma, K. F.: Ozone deposition impact assessments for forest canopies require accurate ozone flux partitioning on diurnal timescales, Atmos. Chem. Phys., 21, 18393–18411, https://doi.org/10.5194/acp-21-18393-2021, 2021.

Walker, A. P., Quaife, T., Van Bodegom, P. M., De Kauwe, M. G., Keenan, T. F., Joiner, J., ... & Woodward, F. I.: The impact of alternative trait-scaling hypotheses for the maximum photosynthetic carboxylation rate (V_{Cmax}) on global gross primary production. *New Phytologist*, *215*(4), 1370-1386, https://doi.org/10.1111/nph.14623, 2017:

Wang, T., Wang, F., Song, H., Zhou, S., Ru, X. and Zhang, H.: Maize yield reduction and economic losses caused by ground-level ozone pollution with exposure-and flux-response relationships in the North China Plain. Journal of Environmental Management, 324, p.116379. https://doi.org/10.1016/j.jenvman.2022.116379, 2022.

Wilkinson, M. D., Dumontier, M., Aalbersberg, I. J., Appleton, G., Axton, M., Baak, A., ... & Mons, B.: The FAIR Guiding Principles for scientific data management and stewardship. Scientific data, 3(1), 1-9. https://doi.org/10.1038/sdata.2016.18, 2016.

Wong, A. Y. H., Geddes, J. A., Ducker, J. A., Holmes, C. D., Fares, S., Goldstein, A. H., et al.: New evidence for the importance of non-stomatal pathways in ozone deposition during extreme heat and dry anomalies. Geophysical ResearchLetters, 49, e2021GL095717, https://doi.org/10.1029/2021GL095717, 2022.

Yen M-Ch. , Peng C-M., Chen T.-C., Chen Ch.-S., Lin N.-H., Tzeng R.-Y., Lee Y.-A. , Lin Ch.-Ch.: Climate and weather characteristics in association with the active fires in northern Southeast Asia and spring air pollution in Taiwan during 2010 7-SEAS/Dongsha Experiment, Atmospheric Environment, Volume 78, Pages 35-50, https://doi.org/10.1016/j.atmosenv.2012.11.015, 2013.

Young, P. J.; Naik, V.; Fiore, A. M.; Gaudel, A.; Guo, J.; Lin, M.; Neu, J.; Parrish, D.; Rieder, H.;Schnell, J. others.: Tropospheric Ozone Assessment Report: Assessment of Global-Scale Model Performance for Global and Regional Ozone Distributions, Variability, and Trends. Elem Sci Anth, 6 (1), https://doi.org/10.1525/elementa.265, 2018.

Zhang, L., Brook, J. R., and Vet, R.: A revised parameterization for gaseous dry deposition in air-quality models, Atmos. Chem. Phys., 3, 2067–2082, https://doi.org/10.5194/acp-3-2067-2003, 2003.

Zhang, W., Feng, Z., Wang, X., Liu, X., & Hu, E.: Quantification of ozone exposure-and stomatal uptake-yield response relationships for soybean in Northeast China. Science of the Total Environment, 599, 710-720, https://doi.org/10.1016/j.scitotenv.2017.04.231, 2017.

Appendix

Table A1: Abbreviations

Symbol	**Long name**
rsmin	Minimum stomatal resistance in [s m^{-1}]
gsmax	Maximum stomatal conductance in [m s^{-1}]
RH	Relative humidity in [%]
LAI	Leaf area index in [m^2 m^{-2}]
sd, sn	snow depth in [m] and snow cover
ssrd, strd	solar and thermal flux at surface in [W m^{-2}]
sw	Soil wetness [m]

al_vis:	albedo (visible)
cwv	canopy water content in [kg m^{-2}]
SWC	Soil water content
SM	Soil moisture [m^3m^{-3}]
wdir	geo wind direction [°]
wspeed	Wind speed in [m s^{-1}]
cv	Vegetation fraction [m^2m^{-2}]
P	Precipitation in [mm]
P_rate	Precipitation rate in [mm h^{-1}], [kg m^{-2} s^{-1}], [m s^{-1}]
Tair, Tsoil, T2m	Air, soil, 2m temperature in [K]
VPD	Vapour pressure deficit [kPa]
Pa	Air pressure [hPa]
Rn, Gr	Net and global radiation [W m^{-2}]
u*	Friction velocity [m s^{-1}]
O_3, CO_2	O_3 and CO_2 concentration in [ppb] und [ppt]
h_dis, z0	Displacement height [m], roughness length [m]
CF	Cloud fraction
LUC	Land usage category